Construction and Building Materials 526 (2026) 146423

Contents lists available at ScienceDirect

Construction and Building Materials

journal homepage: www.elsevier.com/locate/conbuildmat

Drained shear behaviour of recycled construction and demolition waste mixed with natural aggregates and their optimal mix proportion

Nariman Khorsandiardebili, Sanjay Nimbalkar *, Piyush Punetha

School of Civil and Environmental Engineering, University of Technology Sydney, 15 Broadway, Ultimo, NSW 2007, Australia

ARTICLE INFO

Keywords:
Construction and demolition waste
Natural gravel aggregates
Monotonic triaxial test
Drained shear behaviour
Optimal mixture

ABSTRACT

This study investigates the performance of mixed recycled aggregates (MRA) derived from construction and demolition waste (CDW), which incorporates approximately 81% recycled concrete aggregates and 16% crushed brick, when blended with natural gravel aggregates through a comprehensive experimental program. Shear behaviour and dilatancy characteristics of these materials are evaluated within the critical state soil mechanics framework using consolidated drained monotonic triaxial tests. The results reveal that while pure MRA (MRA100) attains higher peak shear strength than pure NGA (NGA100), it also exhibits potential limitations, including the most pronounced strain softening (SS) behaviour, the highest maximum dilation angle (ψ_{max}), and a substantial difference between soaked and unsoaked CBR values (ΔCBR). Incorporating NGA into MRA substantially mitigates these issues, resulting in blends with reduced SS, lower ψ_{max} and smaller ΔCBR compared to MRA100, while achieving higher peak shear strength than NGA100. NGA/MRA mixtures generally exhibit greater effective friction angles than their parent materials (NGA100 and MRA100) under both peak (ϕ'_{peak}) and critical (ϕ'_{cs}) states. With increasing MRA percentage in the mixtures, ϕ'_{peak} increases and ϕ'_{cs} remains relatively constant, but the peak apparent cohesion (c'_{peak}) decreases. Among all mixtures, NGA25/MRA75 emerges as the optimal mix, demonstrating a balance of strength, moisture resilience and ductility. This is evidenced by NGA25/MRA75 exhibiting the highest ϕ'_{peak} and CBR values (both soaked and unsoaked), alongside the lowest ΔCBR, and minimal SS and ψ_{max}. These findings highlight the synergistic benefits of blending recycled CDW with NGA, producing a composite with superior mechanical properties and improved resilience under saturated conditions. By providing critical insights into the engineering behaviour of recycled waste materials, this study supports their broader adoption in transportation infrastructure projects and promotes sustainable construction practices.

1. Introduction

The use of recycled construction and demolition waste (CDW) as an alternative to natural gravel aggregates (NGA) presents significant opportunities, particularly in geotechnical engineering applications, where there is a substantial demand for granular materials. In Australia, the per capita consumption of aggregates stands at approximately 7 tonnes annually [1]. Furthermore, in 2021, the generation of CDW reached approximately 29 million tonnes, of which an estimated 22% was disposed of via landfilling [1,2]. This highlights the necessity to bridge the increasing demand for construction aggregates with the critical challenge of managing them effectively, thereby preventing environmentally harmful landfilling practices and excessive depletion of natural resources.

Over the last few decades, there has been a growing interest in using recycled CDW in transport infrastructure applications, such as pavement bases and subbases [3–9], embankment fills [10–13], backfills for slopes and retaining walls [14–16]. While the integration of CDW into sustainable construction practices seems essential, it is important to gain a proper understanding of its mechanical behaviour compared to conventional natural materials. Recycled CDW is characterised by its inherent heterogeneity and is referred to as mixed recycled aggregates (MRA) in the present study. In general, this composition primarily comprises recycled concrete aggregate (RCA), along with crushed brick (CB), tile, ceramic, mortar, and smaller quantities of wood, glass, plastic, and metal [6,17]. This inherent variability poses a significant challenge for evaluating the performance of MRA, particularly since their primary components, RCA and CB, possess distinctly different physical and

* Corresponding author.
E-mail addresses: Nariman.Khorsandiardebili@student.uts.edu.au (N. Khorsandiardebili), Sanjay.Nimbalkar@uts.edu.au (S. Nimbalkar), Piyush.Punetha@uts.edu.au (P. Punetha).

https://doi.org/10.1016/j.conbuildmat.2026.146423
Received 22 October 2025; Received in revised form 8 January 2026; Accepted 18 April 2026
Available online 23 April 2026

mechanical properties compared to NGA [18].

RCA is typically more porous and has a lower density and higher capacity for water absorption than NGA, primarily due to residual cement mortars that remain attached to its particles [19,20]. This property contributes to their self-cementing capability, which arises from the secondary rehydration of the adhered mortar upon exposure to moisture [21–23]. The self-cementing characteristic of RCA can exhibit significant variability, influenced by its freshness and quality, depending on the material source (i.e., old or new RCA), the quantity of the adhered mortar, and the water exposure time [21,24]. The second major component of MRA, namely CB, is characterised by its lower density, higher crushing value, increased porosity, and greater water absorption compared to RCA [25–27].

Thus, the performance of MRA depends on the relative proportions of its constituents, especially RCA and CB. For instance, Arulrajah et al. [25] reported that incorporating up to 25% CB into RCA and crushed rock blends is feasible for use in pavement subbase applications, as the level of breakage in CB particles remains within acceptable limits up to this proportion. It is therefore crucial to develop a comprehensive understanding of MRA, particularly regarding how their heterogeneity influences the mobilisation of shear strength [18,28,29]. This is especially critical for flexible pavements, where unbound base and subbase materials with higher shear strength have been found to be more effective at reducing rutting [30,31]. Likewise, a knowledge of the shear behaviour of MRA is vital for other applications, such as predicting potential failure of earth structures, including embankments and retaining walls, and ensuring their overall stability [26,32].

So far, investigations into the shear behaviour of MRA have predominantly been conducted through direct shear tests, with a specific emphasis on analysing the interfacial behaviour of these materials [6,33]. However, monotonic triaxial compression tests allow for a more intricate examination of the shear behaviour of heterogeneous materials. While some studies have utilised triaxial tests to examine the behaviour of waste aggregates through fundamental stress-strain and volumetric analysis [34], there is a need for more intricate analyses aimed at gaining a deeper understanding of the complex shear behaviour of heterogeneous materials. In this context, the critical state soil mechanics (CSSM) framework is frequently applied to investigate the stress-dilatancy behaviour of materials with inherent heterogeneity under varying morphology, physical state and loading conditions [35–37]. Using this framework, Zhang and Yang [38] identified that the dilation characteristics of asphalt mixtures are affected by the properties of the aggregates involved, including shape, size and density. Additionally, Yilmaz et al. [39] examined the stress-dilatancy characteristics of binary silica sand blends and found that the fines content and particle size ratio have a significant impact on the critical state parameters of these heterogeneous mixtures.

Specifically focusing on MRA as a highly heterogeneous material, Sarkar and Hegde [40] examined the stress-dilatancy and critical-state behaviour of MRA, in comparison to steel slag, assessing their potential for use in reinforced soil structures. Furthermore, Arulrajah et al. [28] investigated the shear strength and dilatancy characteristics of MRA through consolidated drained triaxial tests. They found that both CB and RCA display a typical shear response akin to coarse-grained soils, with higher dilatancy correlating with increased peak friction angles. Yang et al. [41] also studied the effect of the sphericity of particles on the macroscopic mechanical properties of MRA through a discrete element simulation of a triaxial sample based on the CSSM framework. They revealed that with increasing sphericity, the peak deviatoric stress diminishes. Naeini et al. [42] investigated the stress-dilatancy of MRA mixed with recovered plastics (RP) through a set of monotonic drained triaxial tests. The results indicated that RP content had a notable impact on the compressibility of the MRA, which included RCA and CB. Furthermore, it was observed that CB aggregates exhibited greater breakage potential than RCA particles, a crucial factor that influences the shear strength characteristics of MRA.

It is important to highlight that existing studies on the stress-dilatancy behaviour of MRA have primarily focused on various blends of recycled materials, whereas analyses involving mixtures of MRA with NGA remain scarce. Although a limited number of studies have reported the apparent cohesion and friction angle values of NGA/MRA mixtures [43,44], a significant gap remains in the literature regarding the stress-dilatancy and critical state behaviour of these highly heterogeneous mixtures.

This study aims to investigate the drained shear behaviour and stress-dilatancy characteristics of MRA and NGA individually and compare these findings with results from three NGA/MRA mixtures through a comprehensive experimental program. The effect of MRA content on the dilatancy, peak, and critical state characteristics of the mixtures is thoroughly evaluated, which is the main novelty of this study. Finally, the optimal mixture percentage is identified based on key shear strength parameters. The essential contribution of this study is to provide the rationale for integrating NGA into MRA rather than relying solely on MRA or NGA, through an intricate assessment of their combined performance within the CSSM framework.

2. Methodology

2.1. Basic characterisation

The materials utilised in this study, namely NGA and MRA, were procured from local suppliers in New South Wales, Australia. In general, MRA primarily consists of RCA along with foreign materials such as CB, metal, ceramics, plaster and other impurities. Table 1 presents the typical composition of MRA used in this study, determined in accordance with DTMR Q477 [45] specification. This specification analyses the foreign materials content within MRA materials, which are available alongside the main component, RCA. As indicated in Table 1, the MRA used in this study contains 81.4% RCA and 18.6% of foreign material, including 15.6% CB and 3% other impurities. It is acknowledged that waste streams exhibit inherent variability. Thus, the inherent differences in source, processing and composition contribute to higher heterogeneity of MRA in comparison to NGA. In alignment with established methodologies for fundamental material characterisation (i.e., [43,46]), this study utilises a representative industrial sample from a single batch of a centralised recycling supplier in NSW. This approach effectively isolates the mechanical behaviour of the material itself (including stress-strain, breakage, and dilatancy) from the statistical variability of production, which falls under a future scope of research. However, later in Section 3.8, to determine the optimal mix proportions based on various shear strength properties, a Monte Carlo analysis is conducted. This analysis takes into account the uncertainties which may arise from various factors, including the high intrinsic variability of the waste materials.

In accordance with specifications prescribed by the Department of Transport and Main Roads (DTMR) [47] and the Scenic Rim Regional Council (SRRC) [48], which are specifically tailored for materials suitable for base and subbase layers of flexible pavements, a target particle size distribution (PSD) is established in this study, as illustrated in Fig. 1. All materials, including NGA, MRA, and their mixtures, were sieved and reconstituted to match this target PSD curve, which serves as a unified

Table 1
Typical composition of mixed recycled aggregates (MRA) used in this study.

Material type	Percentage
Recycled concrete aggregates (RCA)	81.4%
Crushed brick (CB)	15.6%
Metal, ceramics and slag (other than blast furnace slag)	1.1%
Plaster, clay lumps and other friable material	0.3%
Rubber, plastic, bitumen (not part of asphalt), paper, cloth, paint, wood and other vegetable matter	0.4%
Asphalt	1.2%

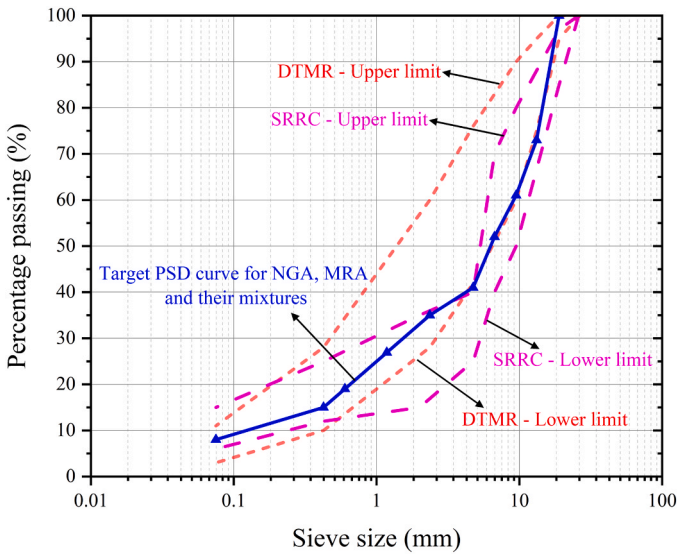

Fig. 1. Target PSD curve for natural gravel aggregates (NGA), mixed recycled aggregates (MRA) and their mixtures, satisfying both DTMR [47] and SRRC [48] criteria.

target gradation, effectively eliminating the influence of gradation variability. As a result, observed differences in shear strength and dilatancy can be attributed solely to the morphological and compositional characteristics of the aggregates, rather than discrepancies in particle size distribution.

Following Australian standards, a complete basic characterisation of NGA and MRA is performed. In addition to standard compaction and CBR tests, aggregate characteristics were analysed through various tests, including the particle density, water absorption, flakiness index, Atterberg limits and organic content test. The results of the basic characterisation tests are summarised in Table 2, accompanied by the relevant standards used. It must be noted that the CBR and compaction test results for the mixtures are discussed in Section ↱3.2.

Table 2 indicates that MRA contains a lower percentage of flaky particles, with a flakiness index (FI) of 5.8%, compared to NGA, which has a FI of 11.7%. It can also be observed that the apparent particle density of MRA is less than that of NGA. Moreover, the water absorption (WA) for MRA is 6.3%, surpassing NGA with a WA of 4.4%. The greater porosity of RCA (along with the adhered cement mortar) and especially CB, present in MRA, may be the reason for reduced density and elevated water absorption of MRA compared to NGA [20,51]. Atterberg limit tests indicate that both NGA and, more notably, MRA contain fines with negligible plasticity. NGA exhibits a low plasticity index (PI) of 3.6%, whereas the MRA fines are non-plastic (i.e., PI = 0). Additionally, both NGA and MRA exhibited minimal shrinkage potential, with linear shrinkage values of 0.6% and 0.7%, respectively. NGA also contains lower organic content (1.2%) than MRA (2.3%).

Table 2
Basic characterisation test results for natural gravel aggregates (NGA) and mixed recycled aggregates (MRA).

Property	NGA	MRA	Standard
Flakiness index, FI (%)	11.7	5.8	DTMR Q201 [45]
Apparent particle density, ρ_s (kg/m^3)	2670	2610	AS 1141.5 [49] & AS 1141.6.1 [50]
Water absorption, WA (%)	4.4	6.3	AS 1141.5 [49] & AS 1141.6.1 [50]
Liquid limit, LL (%)	23.6	28.6	DTMR Q104A [45]
Plastic limit, PL (%)	20	NP[#]	DTMR Q105 [45]
Linear shrinkage, LS (%)	0.6	0.7	DTMR Q106 [45]
Organic content, OC (%)	1.2	2.3	DTMR Q120B [45]
Optimum moisture content, OMC (%)	10.5	14.1	DTMR Q142A [45]
Maximum dry density, MDD (kg/m^3)	2073	1908	DTMR Q142A [45]
CBR (Unsoaked) (%)	124.6	109.3	DTMR Q113C [45]
CBR (4-day soaked) (%)	138.6	158.0	DTMR Q113C [45]

[#] NP = Non plastic

Fig. 2 illustrates a comparison of basic characteristics of NGA and MRA used in this study with those reported in the literature [1,43,46,52,53]. It is apparent from Fig. 2 that the basic properties of NGA and MRA utilised in this study closely align with the upper and lower limits reported in the literature for these materials.

2.2. Monotonic triaxial test

A series of consolidated drained (CD) triaxial compression tests were conducted in this study to investigate the behaviour of NGA, MRA and their mixtures, following ASTM D7181–20 [54]. As shown in Fig. 3, a GDS monotonic triaxial testing apparatus capable of applying confining pressures up to 2 MPa and axial forces up to 40 kN is utilised in this study to conduct a total of 15 CD triaxial compression tests on cylindrical specimens measuring 100 mm in diameter and 200 mm in height. These dimensions ensure that the boundary effects on test results are minimised by maintaining a particle size to diameter ratio greater than 5 [55].

Sample preparation involved careful processing of both NGA and MRA through sieving and classification to achieve the desired PSD, as depicted in Fig. 1, with a maximum particle size limit of 19 mm considered for the parent materials and their mixtures. The aggregates were oven-dried for approximately 24 h at 110 °C and subsequently allowed to equilibrate to room temperature. Water was then added to achieve the desired optimum moisture content (OMC), and the mixture was stored in a sealed container for 24 h to promote uniform moisture distribution. Samples were compacted in five distinct layers at their OMC to achieve maximum dry density (MDD) (with relative compaction exceeding 98%).

For the testing phase, the compacted specimens were placed on a saturated porous disc within the triaxial apparatus, with an additional porous disc positioned on top of each specimen. Filter papers were affixed to porous disks to prevent their clogging. The entire assembly was encased in a 1-mm thick latex rubber membrane and equipped with drainage and pressure monitoring connections (Fig. 3). To facilitate saturation, back pressure and cell pressure were gradually increased while maintaining a constant effective stress on the samples, targeting a minimum Skempton's pore pressure parameter (B value) of 0.95 to ensure full saturation. Once saturated, the specimens were isotropically consolidated at effective confining stresses of 15, 50, and 150 kPa, covering a range from low stress levels typical of near-surface applications (e.g., base or subbase layers) to higher stress levels experienced at larger depths, such as the base of embankment fills [56,57]. Subsequently, drained shear tests were performed at an axial strain rate of 0.05 mm/min to ensure the prevention of excess pore water pressure during shearing [54], with loading continued until an axial strain of 15% was reached.

3. Results and discussion

3.1. Compositional characteristics of NGA100, MRA100 and NGA/MRA mixtures

Before presenting the results, it is essential to describe the compositional characteristics and structural differences of the parent materials and their mixtures examined in this study. This information provides essential context for interpreting the behaviour of the tested materials. As detailed in Section ↱2.1, MRA is inherently heterogeneous, consisting primarily of approximately 81% RCA and 16% CB, with impurities comprising around 3%. For practical purposes, MRA can therefore be treated as a binary mixture by ignoring minor impurities. In contrast,

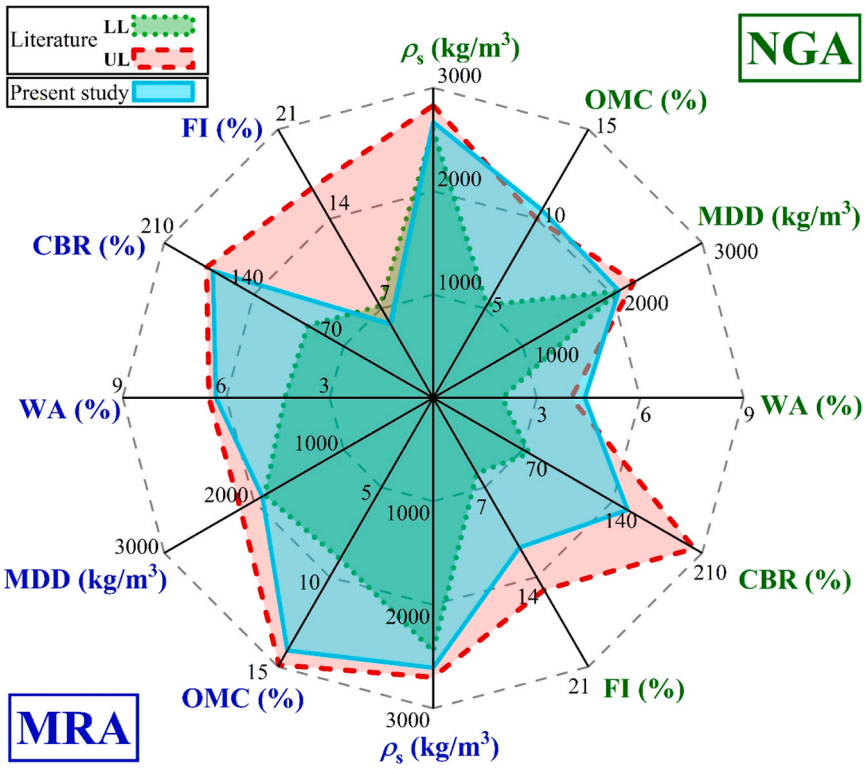

Fig. 2. Comparison of basic characteristics of NGA and MRA in the present study, with lower limit (LL) and upper limit (UL) established from literature data [1,43,46,52,53].

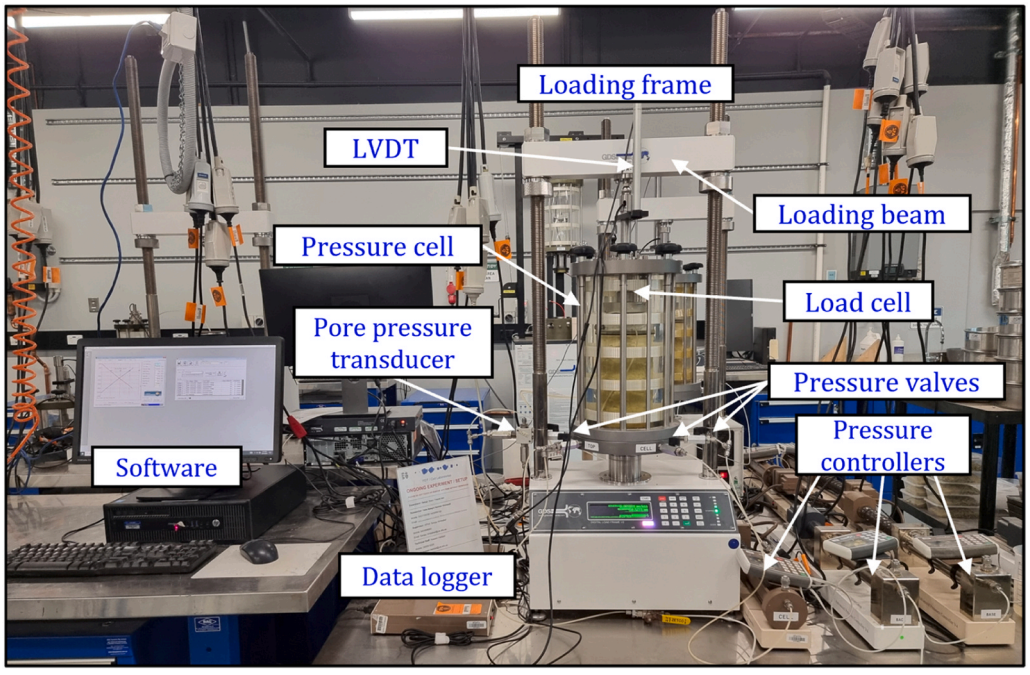

Fig. 3. Monotonic triaxial test apparatus used in this study.

NGA is comparatively homogeneous. These fundamental differences cause pronounced morphological and structural contrasts between the pure-material specimens, namely NGA100 and MRA100, which are also referred to as the "parent materials".

When NGA and MRA are combined in proportions of 25%, 50%, and 75%, the resulting composites constitute ternary mixtures, namely NGA, RCA and CB. Accordingly, the parent materials serve as benchmarks for evaluating the performance of the NGA/MRA mixtures. The term "mixtures" in this study explicitly refers to NGA75/MRA25, NGA50/MRA50, and NGA25/MRA75. Trends associated with increasing MRA content are analysed for the "mixtures" and compared relative to the results of "parent materials". This explicit differentiation of material nature (namely, homogeneous NGA, binary MRA, and ternary NGA/MRA mixtures) enables a more realistic assessment and supports a

nuanced interpretation of the observed geotechnical behaviour. In the same context, the term "materials" refers to both parent materials and mixtures in a generic manner.

3.2. Compaction and CBR test results

Fig. 4 illustrates the dry density–moisture content relationships for pure NGA and MRA, as well as their blends, alongside the corresponding values of OMC and MDD for each material. It is evident that NGA100 exhibits the highest packing ability among all tested materials, achieving the highest MDD of 2073 kg/m^3 and the lowest OMC of 10.5%. In contrast, MRA100 shows the lowest MDD at 1908 kg/m^3 and the highest OMC at 14.1%.

With increasing the MRA percentage in the mixtures, OMC increases, while the packing capability degrades, as evidenced by the observed decrease in MDD. The lower MDD of the mixtures compared to NGA100 can be attributed to the lower apparent particle density (see Table 2) as well as higher angularity of MRA particles which increases the void ratios of the mixtures [58]. Furthermore, due to the enhanced water absorption characteristics of MRA particles (see Table 2), a greater amount of water is required to achieve optimal compaction for the mixtures in comparison to NGA100.

Fig. 5 presents a comparative analysis of the unsoaked and 4-day soaked CBR values, along with their differences, for NGA100, MRA100, and their mixtures. Notably, MRA100 achieves the highest soaked CBR value of 158% among all tested materials; however, it exhibits the lowest unsoaked CBR value of 109.3% [Fig. 5(a)]. The mixtures exhibit an increasing trend in both soaked and unsoaked CBR values as the percentage of MRA increases. Furthermore, NGA25/MRA75 demonstrates superior unsoaked CBR values compared to both NGA100 and MRA100, while its soaked CBR is roughly comparable to MRA100 and exceeds that of NGA100.

The difference between the soaked and unsoaked CBR values (ΔCBR), illustrated in Fig. 5(b), reflects the sensitivity of each mixture to saturation and moisture variation. NGA100 demonstrates the lowest sensitivity, evident through the smallest ΔCBR value, while MRA100 exhibits the highest sensitivity, with a difference of approximately 49%. This indicates that the strength of MRA100 increases significantly when soaked in water for 96 h. However, at its OMC state (i.e., unsoaked condition), the least CBR value is observed for MRA100, even lower than that of NGA100. The elevated soaked CBR values and the significant disparity between soaked and unsoaked CBR in the MRA100 samples,

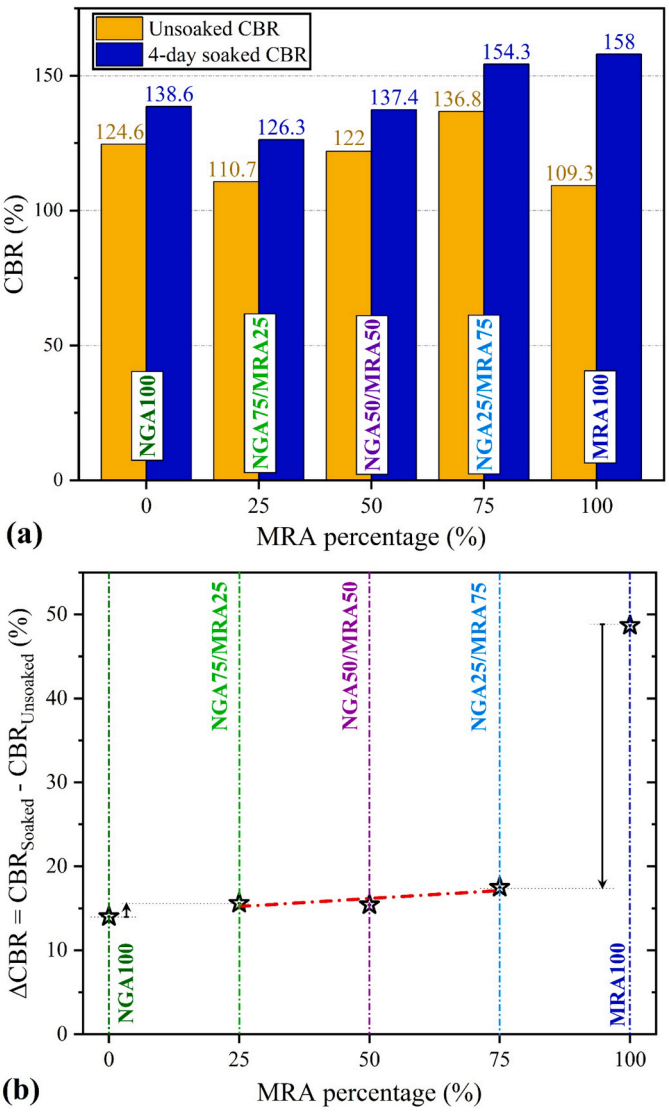

Fig. 5. (a) Unsoaked and 4-day soaked CBR test results; (b) differences between soaked and unsoaked CBR values, both plotted against the percentage of MRA in the mixtures.

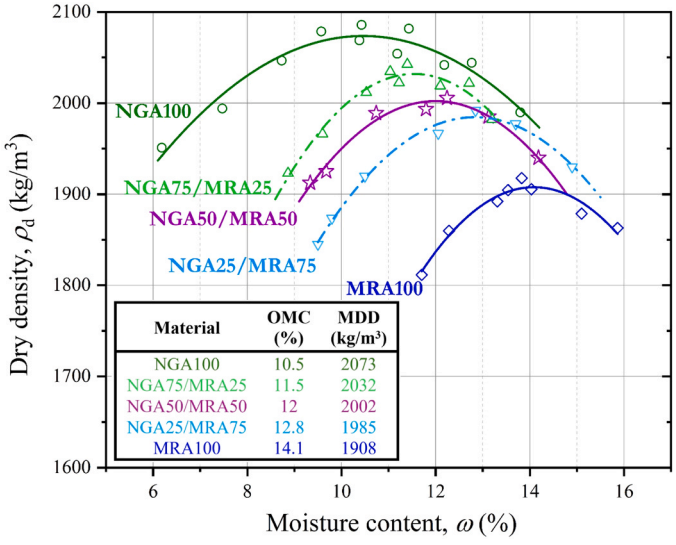

Fig. 4. Relationship between dry density and moisture content for the parent materials and their mixtures.

which are rich in RCA, can be attributed to the secondary hydration of unhydrated cement particles present in the adhered mortar upon exposure to water during the soaking phase [21–23,40]. The four-day soaking period, an essential component of the soaked CBR test, serves effectively as a curing phase that promotes the rehydration process. Comparably, Martinez-Echevarria et al. [59] documented great differences between soaked and unsoaked CBR values, reporting an unsoaked CBR of 120% and a soaked CBR of 242%, reflecting an impressive increase of up to 122%. Furthermore, their findings indicated that prolonging the soaking period can further elevate CBR values across various types of mixed RCA. In contrast, for natural aggregates, they reported relatively modest differences in CBR values, typically less than 13%, regardless of the soaking duration.

As the percentage of MRA in the mixtures increases, the differences in CBR values also rise marginally, indicating a slightly higher sensitivity to moisture variations [see Fig. 5(b)]. However, a significant disparity exists between the moisture sensitivities of MRA100 and the mixtures. The incorporation of non-plastic NGA fines appears to disrupt the cementitious bonding within the RCA particles in MRA, leading to reduced sensitivity in the mixtures. Furthermore, the strength in these mixtures appears to shift primarily towards the interlocking of particles

coupled with the filling of voids resulting from the breakage of weaker MRA particles by stiffer NGA particles. Increasing the MRA percentage in the mixtures to 75% yields a robust combination that outperforms NGA100 in its unsaturated OMC state. Thus, NGA25/MRA75 emerges as the most stable mixture, demonstrating elevated CBR values in both soaked and unsoaked states, along with minimal variation in strength under moisture variations. It must be noted that all blends exhibited negligible swelling during the soaking tests.

In subsequent sections, a comprehensive discussion on the monotonic triaxial test results is provided that delves deeper into the physical phenomena governing the shear behaviour of the mixtures and their parent materials.

3.3. Introduction to stress-dilatancy behaviour of NGA/MRA mixtures

Fig. 6 illustrates a typical stress–dilatancy relationship for an NGA/MRA mixture. A comparable trend is consistently observed across all NGA/MRA mixtures and at various confining stress levels in this study (as demonstrated later in Sections ↱3.4 and ↱3.5), highlighting their alignment with the behaviour of the parent material MRA100, along with NGA100. Figs. 6(a) and 6(b) depict the relationships of deviatoric stress (q, where $q = \sigma'_1 - \sigma'_3$; σ'_1 and σ'_3 are the major and minor effective principal stresses, respectively) and volumetric strain (ε_v), respectively, with axial strain (ε_a). Furthermore, Fig. 6(c) depicts a typical stress ratio–dilatancy plot of a mixture. The stress ratio (η) is defined as the ratio of deviatoric stress to mean effective stress [p', where $p' = (\sigma'_1 + 2\sigma'_3)/3$], represented by $\eta = q/p'$. Dilatancy denotes the rate of volumetric change that occurs during shearing in relation to the change in deviatoric strain, as expressed by the following equation:

$$D = \frac{d\varepsilon_v}{d\varepsilon_q} \tag{1}$$

where D is the dilatancy parameter, $d\varepsilon_v$ represents the increment in volumetric strain, and $d\varepsilon_q$ denotes the increment in deviatoric strain. The volumetric and deviatoric strains are calculated as follows:

$$\varepsilon_v = \varepsilon_a + 2\varepsilon_3 \tag{2}$$

$$\varepsilon_q = \frac{2}{3}(\varepsilon_a - \varepsilon_3) \tag{3}$$

where ε_3 refers to the radial strain. It must be noted that the contraction is considered positive in this study, while dilation is regarded as negative, in accordance with the soil mechanics conventions.

Dilatancy can also be inferred from Fig. 6(b) by examining the trend in the tangential slope of the volumetric strain-axial strain graph (m). Zero dilatancy can be represented by a tangential slope of zero in Fig. 6 (b), while maximum dilatancy (D_{max}) is related to the tangential slope at its maximum absolute value, occurring at point D*. Fig. 6 also illustrates some key phases during the shearing process that facilitate a better understanding of the material response, as discussed in the subsequent sections.

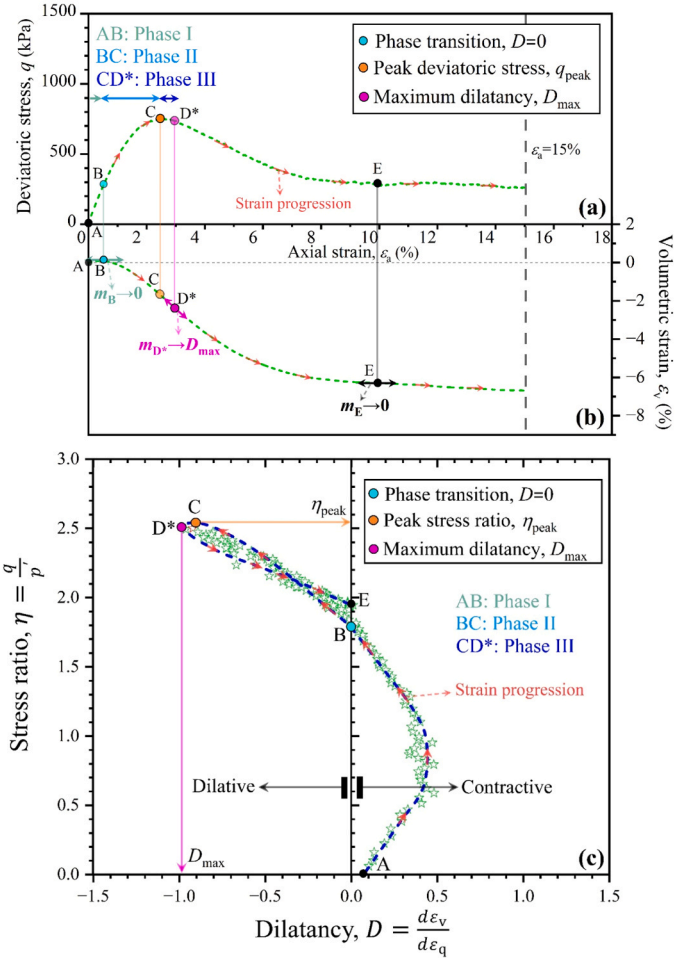

Fig. 6. Schematic representation of the change in (a) deviatoric stress with axial strain; (b) volumetric strain with axial strain; and (c) stress ratio with dilatancy for a typical NGA/MRA mixture specimen tested in this study.

3.3.1. Pre-peak behaviour

3.3.1.1. Phase I. In the first phase, which commences when the samples are subjected to shearing (point A in Fig. 6) in CD triaxial tests, the sample begins to contract, showing positive volumetric strain [see Fig. 6 (b)]. During this phase, along with the volumetric contraction, the shear strength begins to mobilise, as illustrated in Fig. 6(a). The contraction persists until it reaches the phase transition point (point B), where the dilatancy value shifts from positive to zero ($D_B = 0$) and then to negative, indicating a change in the behaviour of the material from contractive to dilative [Fig. 6(c)].

3.3.1.2. Phase II. This phase commences when the samples begin to dilate [point B in Fig. 6] under shearing and continues until the maximum deviatoric stress is reached (point C in Fig. 6). It is noted that, under a given confining stress, the peak stress ratio (η_{peak}) typically occurs at the same axial strain as the peak deviatoric stress (q_{peak}). As can be seen in Fig. 6(b), during this phase, as ε_a increases, q increases, and the sample exhibits continuous dilation [Fig. 6(c)], reflected as a continuous increase in absolute volumetric strain [Fig. 6(b)] until the peak stress state is reached. During this phase, although dilatancy increases, it has not yet surpassed the maximum dilatancy state.

3.3.2. Post-peak behaviour

3.3.2.1. Phase III. This phase commences at the peak stress state and extends until the maximum dilatancy is achieved [point D* in Figs. 6(a) and 6(b)]. During this period, the sample continues to exhibit dilation, reaching its greatest dilatancy value (D_{max}). D_{max} is correlated with the maximum dilation angle of a sample, which will be presented in Section ↱3.7. It is important to note that, at this stage, dilation is accompanied by strain softening (SS), meaning that the corresponding point on the stress-strain curve reflects a deviatoric stress that is lower than q_{peak}. As observed in Fig. 6(c), after the peak point in stress-dilatancy space, a hook-shaped return to the direction of lower stress ratio in the curves is observed, similar to the behaviour reported by Jin et al. [60] for crushable calcareous sands, which exhibited a downward hook turn.

3.3.2.2. Softening behaviour and critical state. Upon reaching the

maximum dilatancy, the softening behaviour persists as deviatoric stress diminishes until it stabilises to a nearly constant residual level [Fig. 6 (a)]. During this period, the volumetric strain ultimately achieves a point where the dilatancy rate becomes zero [$D_E = 0$, shown in Figs. 6(b) and 6(c)], commonly referred to as the critical state in soils that do not exhibit localised failure [61]. In instances where the deformation patterns in samples are associated with the onset of localisation, which does not reflect a uniformly deformed state [62], it is inappropriate to extrapolate the critical state from just one dataset. To accurately determine the critical state for samples displaying visible shear band localisation, it is crucial to conduct multiple tests under varying confining stresses [39,63]. Therefore, in this study, with shear band localisation observed in the samples (as depicted in Fig. 7), the critical state is determined based on the results of tests conducted under multiple confining stresses of 15, 50, and 150 kPa. This aspect will be further elaborated and analysed in detail for NGA100, MRA100, and their mixtures in Section ↱3.5.

3.4. Stress-strain analysis and volumetric behaviour

Fig. 8 depicts the drained shear behaviour of all the materials tested in this study, illustrating the relationships between q, ε_a and ε_v across various σ'_3 of 15, 50, and 150 kPa. The maximum contractive volumetric strain at which the mixture begins to dilate, referred to as the phase transition point (Phase I in Section ↱3.3.1.1), increases with an increase in σ'_3 [see Figs. 8(b), 8(d), 8(f), 8(h) and 8(j)]. Conversely, the trend is reversed for dilative volumetric change; as σ'_3 increases, the extent of dilative volumetric change decreases. This indicates that elevated confinement results in greater contraction of the materials, while simultaneously reducing the extent of dilation during the dilation phase. Furthermore, it is observed that the phase transition point occurs at higher axial strain levels with increasing σ'_3. This indicates that contractive volumetric changes are not only more pronounced but also persist for a longer period under elevated confinement. The corresponding phase transition points in stress-strain space demonstrate that as σ'_3 increases, their associated deviatoric stress also rises [see Figs. 8 (a), 8(c), 8(e), 8(g) and 8(i)]. Overall, until the phase transition, increased confinement enables the mixtures to attain higher deviatoric stress, while volumetric contraction is intensified and shifts to higher axial strain levels

Furthermore, an increase in σ'_3 is associated with an increase in q_{peak} across all materials [see Figs. 8(a), 8(c), 8(e), 8(g), and 8(i)]. It is noteworthy that to ensure reproducibility of the results, three different specimens of the same material (i.e., NGA100) were assessed through triaxial tests, all of which were prepared and sheared under identical conditions. The assessment revealed a maximum stress variation of ±5%. The corresponding values for q_{peak} and SS under different σ'_3 for all five materials are shown in Table 3. It is apparent from Table 3 that SS becomes more pronounced with increasing σ'_3, as indicated by the increased difference between q_{peak} and residual state strength (q_{res}). This indicates that, until reaching the peak state (Phase II in Section ↱3.3.1.2), elevated confinement enables the mixtures to withstand higher deviatoric stresses, albeit with a more brittle behaviour, evidenced by a greater post-peak strength reduction before reaching the residual state. It can also be observed that under elevated confinement, the peak stress points are shifted to higher axial strain levels, and the corresponding dilative volumetric strains are reduced.

Finally, at the end of Phase III, as σ'_3 increases, D_{max} decreases while their corresponding deviatoric stress level increases (see Fig. 8). In other words, at higher confinement, the mixtures exhibit a lower maximum dilatancy while concurrently experiencing higher deviatoric stress in the stress-strain space. This trend will be more clearly observed in Section ↱3.5, which illustrates the stress-dilatancy behaviour of the materials.

It can be observed from Table 3 that MRA100 consistently exhibits the highest q_{peak} compared to other mixtures and NGA100, irrespective of the confining stress levels. This may be attributed to the higher sphericity of NGA particles compared to MRA. Previous studies have also reported that an increase in particle sphericity results in a decrease in q_{peak} [41]. In addition, MRA100 and NGA100 demonstrate the highest and lowest strain softening, respectively, highlighting the potential risk of using pure MRA due to its sharper post-peak strength drop compared to pure NGA. This represents the brittle behaviour of MRA, as also reported by Naeini et al. [42]. This phenomenon may be attributed to the deterioration of the apparent cohesion due to the failure of self-cementing bonds between RCA particles within MRA, following the peak state [21,22,64,65]. In other words, MRA100 transitions from a pre-peak cohesive-frictional behaviour, where apparent cohesion is attributed to high RCA content and the rehydration of residual cement mortar, to a post-peak frictional behaviour due to the deterioration of self-cementation bonds. On the other hand, NGA100, which includes non-plastic fines, lacks this additional mechanism of cohesion and bonding. The significance of self-cementation bonds in enhancing the apparent cohesion of MRA100 is further elaborated in Section ↱3.6, where MRA100 displays the highest level of apparent cohesion

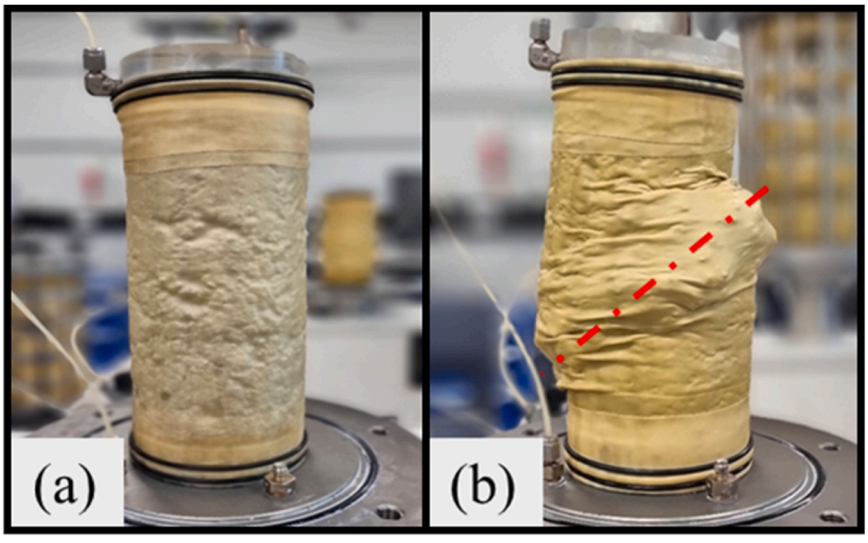

Fig. 7. Evolution of a typical NGA/MRA mixture during the monotonic triaxial test: (a) sample before shearing; (b) sample at 15% axial strain (end of the test) showing a localised shear band.

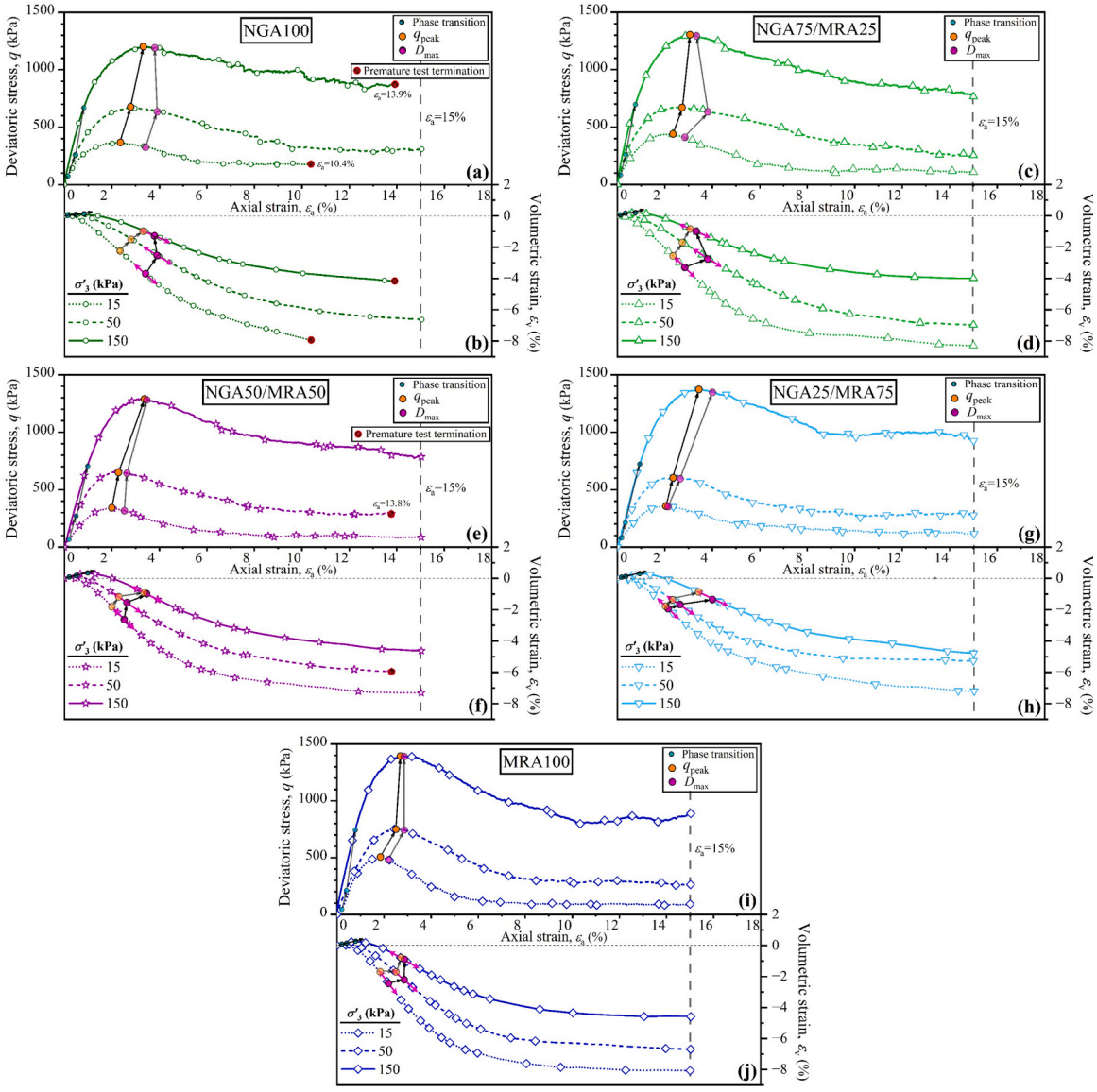

Fig. 8. Stress-strain relationships and volumetric strain variations with axial strain for different mixtures: (a, b) NGA100; (c, d) NGA75/MRA25; (e, f) NGA50/MRA50; (g, h) NGA25/MRA75; and (i, j) MRA100.

compared to NGA100 and the mixtures.

In addition to Table 3, Fig. 9 more clearly illustrates the variation of SS with MRA content and σ'_3. Although SS increases with rising σ'_3, as previously demonstrated, it exhibits a decreasing trend with increasing MRA content across the mixtures. This relationship is represented through a fitting surface in Fig. 9, developed for three mixtures under three different σ'_3 of 15, 50, and 150 kPa. These observations suggest that although MRA100 showed the potential for a significant reduction in post-peak strength compared to NGA100, the incorporation of NGA into MRA significantly mitigates the SS effect, irrespective of σ'_3 levels.

Specifically, the NGA25/MRA75 mixture exhibits the lowest SS, among all three mixtures, demonstrating the most significant reduction in SS with respect to MRA100 (see Fig. 9 and Table 3). In fact, relative to MRA100, NGA25/MRA75 exhibits a reduction in SS of approximately 42%, 34%, and 29% under σ'_3 of 15, 50, and 150 kPa, respectively. Accelerated crushing of weaker components in the mixtures [66], namely MRA particles, may be the reason for such reduced post-peak strength loss (lower SS). Shen et al. [67] also reported that an increase in particle breakage in a gravelly sand mixture results in a reduction in post-peak strain softening.

As illustrated in Table 3, the axial strain corresponding to the peak state (ε_a^{peak}) for MRA100 is lower than that for NGA100, irrespective of σ'_3. This phenomenon may be attributed to the pronounced asperities and rough MRA particles, which promote the rapid mobilisation of interlocking resistance at low strain levels. In contrast, the delayed peak in NGA100 reflects strength mobilisation dominated by frictional sliding and particle rearrangement, requiring larger axial strains to fully mobilise strength.

Regarding the mixtures, no specific trend was observed for ε_a^{peak} with varying MRA content, as the behaviour differed depending on the level of σ'_3. Nevertheless, it is evident that the mixtures generally exhibit lower ε_a^{peak} than NGA100 while showing higher ε_a^{peak} than MRA100, particularly for lower percentages of MRA in the mixtures, such as NGA75/MRA25 and NGA50/MRA50.

3.5. Stress-dilatancy relationship and critical state

Fig. 10 illustrates the relationship between dilatancy and stress ratio for parent materials and their three mixtures under varying σ'_3. A consistent trend is observed across all materials: As σ'_3 increases, the

Table 3
Results for peak stress (q_{peak}), strain softening (SS), peak stress ratio (η_{peak}) and the corresponding axial strain to peak state (ε_a^{peak}), maximum dilation angle (ψ_{max}), and excess friction angle (ϕ'_{ex}) for the parent materials and their mixtures under confining pressures (σ'_3) of 15, 50, and 150 kPa.

Parameter	σ'_3 (kPa)	MRA percentage (%)				
		0	25	50	75	100
		NGA100	NGA75/MRA25	NGA50/MRA50	NGA25/MRA75	MRA100
q_{peak} (kPa)	15	367.5	439	336.9	356.4	501.1
	50	671.6	673.4	654.3	604.9	751
	150	1199.4	1301	1292.5	1371.5	1393.1
SS[#] (kPa)	15	194.2	329	252.6	241.8	414.3
	50	361.8	421.8	368.7	322.8	489.8
	150	339	513.9	497.5	373.9	523.5
ε_a^{peak} (%)	15	2.33	2.33	2.00	2.08	1.85
	50	2.83	2.65	2.27	2.38	2.50
	150	3.37	3.10	3.37	3.40	2.70
η_{peak}	15	2.67	2.72	2.65	2.66	2.75
	50	2.45	2.45	2.44	2.40	2.50
	150	2.18	2.23	2.23	2.26	2.27
ψ_{max} (°)	15	27.1	29.2	28.8	26.7	34.6
	50	19.5	22.0	25.1	22.7	29.1
	150	17.5	18.0	19.7	18.2	20.2
ϕ'_{ex} (°)	15	20.8	20.6	20.1	18.4	23.8
	50	13.7	11.7	13.6	10.2	15.1
	150	6.3	5.5	7.7	6.3	8.5

[#]SS = $q_{peak} - q_{res}$; where q_{res} is the deviatoric stress corresponding to the residual state.

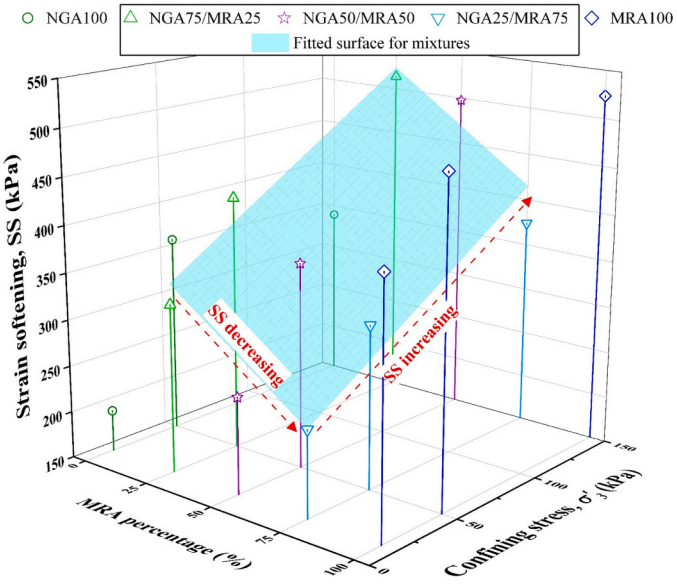

Fig. 9. Variation of strain softening versus MRA percentage and confining stress.

peak stress ratio (η_{peak}) decreases, which contrasts with the previously observed increasing trend of q_{peak} (see Section ↱3.4). Table 3 also lists the corresponding values of η_{peak} for each mixture under different σ'_3.

It is important to elaborate that η_{peak} does not represent an absolute strength value but rather reflects the efficiency with which a material mobilises its internal resistance to shearing under various stress levels, while q_{peak} indicates the absolute load-bearing capacity of the sample at failure. NGA100, MRA100, and their mixtures demonstrate lower η_{peak} and thus smaller mobilised strength levels under higher σ'_3, despite possessing potentially higher inherent shear strength capacities. It is noteworthy that η_{peak} is typically attained concurrently (at the same axial strain) with q_{peak}. Notably, alongside the highest deviatoric stress values, MRA100 consistently demonstrates the highest η_{peak} when compared to NGA100 and the mixtures. This observation indicates the superior ability of MRA100 to mobilise higher shear strength.

Following Section 3.3.2.2, the critical state is obtained by extrapolating the $\eta-D$ relationship beyond η_{peak}. This is performed by fitting the post-peak stress-dilatancy data using Nova's linear formulation and extrapolating the critical state stress ratio, M_{cs}, through the fitted trend line [39,68]. The intercept of this line with the η-axis defines M_{cs} [$\eta=M_{cs}+(1\text{-}N)D$, where N is a coefficient of volumetric coupling]. As shown in Fig. 10, M_{cs} is determined for each material composition and lies in a narrow range across all materials (1.92–2.01), indicating minor variability in critical state strength, in contrast to the broader dispersion observed in peak stress ratios (Table 3). In addition to M_{cs}, which maps directly to the critical state friction angle for each material composition (parent materials and blends), the values of η_{peak} can be interpreted as the peak friction angle independent of confining stress. This framework supports the assessment of how both critical state and peak strength parameters vary with MRA content, which is examined in the next section.

As illustrated in Fig. 10, the results for M_{cs} indicate that MRA100 exhibits the highest coefficient of determination (R^2) and the lowest deviation of the data from the trend line across three confining stresses. Most deviations in the post-peak data for the mixtures appear to arise from the low confining stress post-peak responses, particularly when confining stresses are below 50 kPa, where the sample response is highly sensitive to its initial structural and morphological condition, which varies significantly among the mixtures, as previously discussed. Furthermore, it is important to note that this study employs Nova's method [39,68], explicitly proposing a linear regression approach to extrapolate the post-peak stress-ratio–dilatancy relationship in materials exhibiting shear localisation under various confining stresses. In this context, the observation of low R^2 values aligns with the understanding that shear localisation results in distinct post-peak critical state values across different tests conducted under varying confining stresses. If the post-peak data highly converge, leading to a high R^2 value, this would imply that the samples attained similar critical state stress ratios, indicating that a relatively uniform strain distribution is present and that the results from a single test may suffice for deriving the critical state stress ratio. Thus, for samples exhibiting visible shear bands where the post-peak data is scattered, a composite critical state value can be derived by aggregating the data and applying a fitted linear regression, yielding a more realistic estimate of the critical state stress ratio

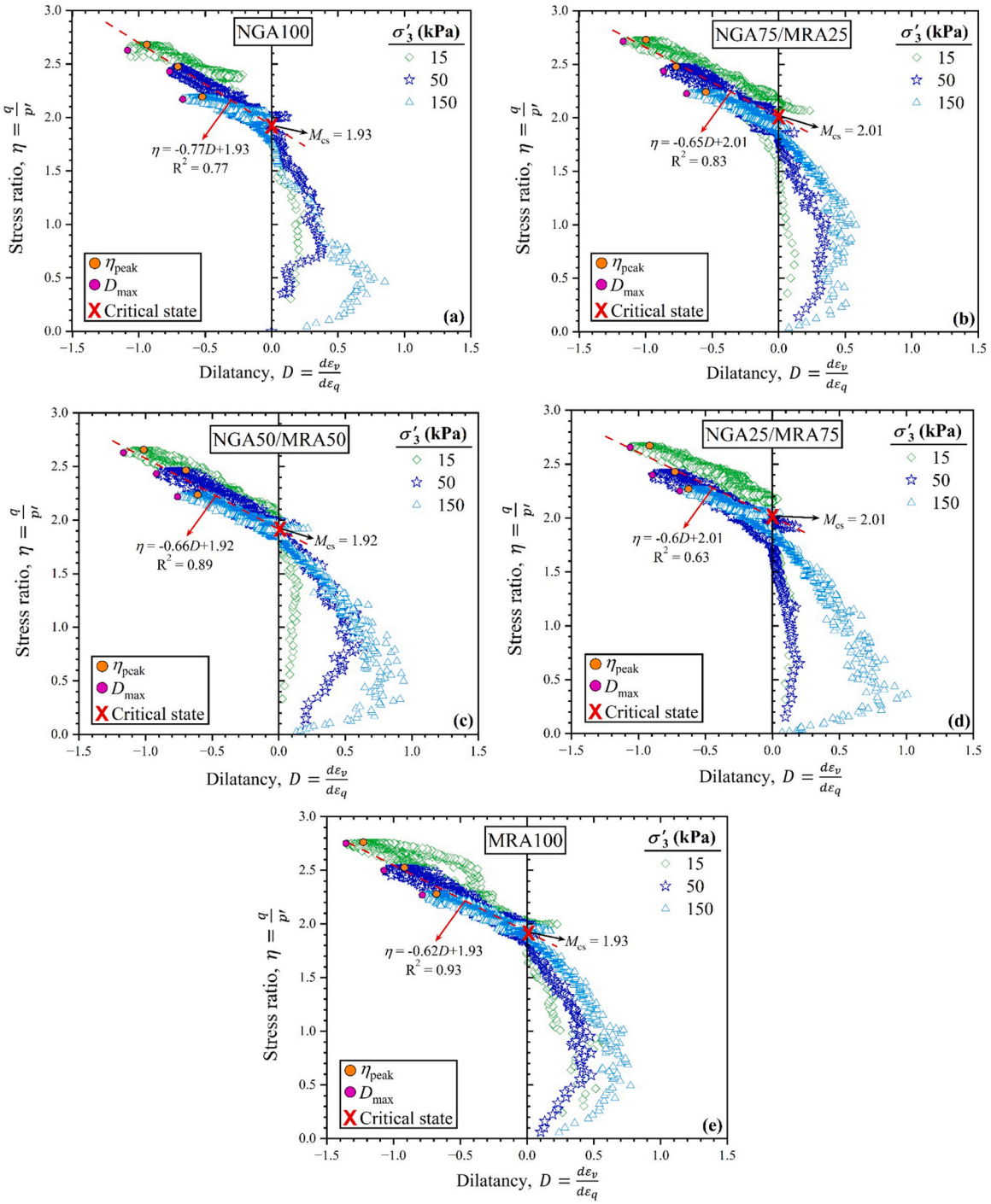

Fig. 10. Stress ratio vs dilatancy relationship for the different mixtures: (a) NGA100; (b) NGA75/MRA25; (c) NGA50/MRA50; (d) NGA25/MRA75; and (e) MRA100.

3.6. Peak state friction and cohesion, and critical state friction angle

In the q-p' space, two key reference lines are established from the CD triaxial data: peak and critical state lines. For each material, the results of three tests at σ'_3 of 15, 50 and 150 kPa are used to locate the corresponding peak-state points in the q-p' plane. A linear fit through these points defines the peak state line as:

$$q = M_{peak}\, p' + k \tag{4}$$

where M_{peak} is the slope and k is the intercept at $p'= 0$, which are correlated with the peak effective friction angle (ϕ'_{peak}) and peak apparent cohesion (c'_{peak}) of the tested materials, respectively. ϕ'_{peak} and c'_{peak} are calculated as follows:

$$\phi'_{peak} = \sin^{-1}\left(\frac{3M_{peak}}{6 + M_{peak}}\right) \tag{5}$$

$$c'_{peak} = k\left(\frac{3 - \sin\phi'_{peak}}{6\cos\phi'_{peak}}\right) \tag{6}$$

Additionally, the critical state line is derived based on the critical state stress ratio (M_{cs}), which is extrapolated from the results of the post-peak behaviour in η–D space (refer to Sections ↱3.3.2.2 and ↱3.5). M_{cs} is the slope of the critical state line in q-p' space passing through the origin, which is utilised to calculate the critical state friction angle (ϕ'_{cs}) as

follows:

$$\phi'_{cs} = \sin^{-1}\left(\frac{3M_{cs}}{6+M_{cs}}\right) \quad (7)$$

Table 4 presents the values of ϕ'_{peak}, ϕ'_{cs} and c'_{peak} for all materials, while Fig. 11 illustrates how MRA content influences these parameters in the mixtures compared to NGA100 and MRA100. The results indicate that MRA100 exhibits a higher peak friction angle (ϕ'_{peak}= 50°) compared to NGA100 (ϕ'_{peak} = 48.7°). Notably, ϕ'_{peak} values of all mixtures exceed that of NGA100. Except for NGA75/MRA25, other mixtures exhibited higher ϕ'_{peak} than MRA100, with the NGA25/MRA75 mixture achieving the highest value at 52.2° among all tested materials. Fig. 12 illustrates a typical sample of NGA50/MRA50 from a morphological perspective. As can be seen, MRA particles, including its main component, RCA, generally exhibit a rougher surface texture with more asperities compared to NGA particles. RCA is characterised by significant surface roughness, primarily attributed to the presence of a cement layer and residual old mortar [69]. Furthermore, Mikhailenko et al. [70] indicated that the phenomenon of intergranular locking, coupled with the inherent roughness of coarse aggregates, is more pronounced in RCA compared to conventional aggregates. Such increased intergranular locking may contribute to a higher ϕ'_{peak} in MRA100 compared to NGA100. As the proportion of MRA in the mixtures increases, the interactions among the rougher particles with enhanced asperities lead to a further increase in ϕ'_{peak}. Previous studies have also demonstrated that surface asperities facilitate greater interlocking among particles while limiting their rotational motion [71–73], ultimately resulting in an increase in peak shear strength at the macro scale. However, a precise microstructure assessment of MRA particles through scanning electron microscopy (SEM) for capturing surface textures and remnant cement mortars, along with quantitative shape analysis, may yield valuable insights into the behaviour of these materials. Implementing these methodologies is recommended for the further development of this study, as they can enhance our understanding of the fundamental properties and performance of MRA in various applications.

The range of ϕ'_{peak} and c'_{peak} values observed in this study for NGA/MRA mixtures and the parent materials (Table 4) is consistent with those reported in the literature [28,29,43,44], showing a range from 48 to 54.58° for ϕ'_{peak} and a variation between 41 and 87.4 kPa for c'_{peak}.

Regarding ϕ'_{cs}, MRA100 and NGA100 show comparable values. Although the mixtures exhibit a relatively stable trend with increasing MRA percentages, they maintain higher levels of ϕ'_{cs} values compared to their parent materials. ϕ'_{cs} is typically represented as the sum of two components: interparticle friction and particle rearrangement. The interparticle friction is governed by particle roughness, mineralogy and contact characteristics [74,75], and is largely insensitive to initial density and confining pressure, whereas the rearrangement term reflects fabric evolution and dilatancy, and depends on both the initial density and the level of confinement [76,77]. Relative to the parent materials, the mixtures exhibit a synergistic response: they achieve greater packing efficiency (higher density) than MRA100 and stronger particle interlocking than NGA100 due to the incorporation of rougher, asperity-rich MRA particles. Consequently, the mixtures mobilise a higher ϕ'_{cs} and outperform the parent materials, which have relatively comparable critical-state behaviour. Overall, the results demonstrate that both ϕ'_{peak} and ϕ'_{cs} of the mixtures increase relative to their parent materials.

Table 4
Peak and critical state shear strength parameters.

Materials	ϕ'_{peak} (°)	c'_{peak} (kPa)	ϕ'_{cs} (°)
NGA100	48.7	59.4	46.8
NGA75/MRA25	49.5	64.2	48.8
NGA50/MRA50	51.0	46.6	46.6
NGA25/MRA75	52.2	40.4	48.9
MRA100	50.0	74.7	46.8

However, in terms of c'_{peak}, a decreasing trend is observed in the mixtures with increasing MRA percentage, while both parent materials, MRA100 and NGA100, typically show higher cohesion values than the mixtures. MRA100 shows significantly higher c'_{peak} of 74.7 kPa compared to NGA100 and the mixtures. The non-plastic NGA fines and coarse NGA particles (lacking unhydrated cement) interfere with the formation of cementitious bonds among MRA particles. This interference weakens the mechanisms that contribute to apparent cohesion and leads to more ductile behaviour, resembling that of NGA100. This phenomenon is further supported by the CBR test results discussed in Section 3.2, indicating that incorporation of NGA into MRA minimises the difference in soaked and unsoaked CBR values in the mixtures, a difference that was significant in MRA100.

Unlike NGA100, MRA100 possess RCA particles with remnant attached mortars (see Fig. 12) that form cementitious bonds when exposed to water. Furthermore, previous studies found that the inclusion of weaker particles within a granular assembly results in their preferential breakage under mechanical loading [66,78]. The higher crushability of MRA components was quantitatively confirmed by Zhu et al. [79] who found that CB exhibits a very high crushing value of 42.3%, which is more than double and triple that of RCA and NGA, respectively. Thus, NGA particles serve as a grinding medium for MRA, resulting in a greater degree of breakage of MRA particles within the mixtures compared to a pure MRA sample, where stresses are distributed more uniformly among particles of comparable strength. Within a mixed granular skeleton, high contact stresses are concentrated at the sharp corners of weaker MRA particles in contact with more rigid NGA particles. A similar observation was reported by Nimbalkar et al. [80] that highly angular fresh ballast particles witnessed localised breakage due to significant nonuniform high stress concentrations at their corners. Thus, stress concentrations, along with the propensity of weaker components to break preferentially, may lead to the crushing of CB and attrition of RCA particles, as well as the failure of cementation bonding, which is an identified breakage mechanism in RCA [69]. This entire process can inhibit the formation of a cemented matrix, disrupting the apparent cohesion mechanism.

Nevertheless, it is pertinent to elucidate the notion of apparent cohesion from multiple perspectives: firstly, employing a linear regression of peak stress ratios at different confining stress may result in overestimation of the real apparent cohesion, as the failure envelope tends to exhibit a nonlinear pattern [81–83], especially at lower stress levels. Thus, in practice, the apparent cohesion of different mixtures may vary within a narrower range. To address this concern, multiple triaxial tests should be performed at various confining stress levels for each mixture, enabling the derivation of a modified nonlinear failure envelope, which is suggested as a promising direction for further research.

Secondly, while MRA may exhibit apparent cohesion due to its shape and self-cementing properties, especially before reaching the peak state, the practical implications of such apparent cohesion may require a cautious approach, as the apparent cohesion in MRA mixtures is significantly influenced by factors such as moisture content and compaction level of the sample, and the source of the materials [84,85]. Furthermore, variations in the percentage of RCA and CB within a MRA mixture can lead to significant fluctuations in apparent cohesion [86]. Arisha et al. [86] and Azam and Cameron [84] reported that even with minor changes in either composition of the MRA mixture or moisture content, apparent cohesion may have significantly different values. This variability suggests that relying on apparent cohesion for stability assessments may result in inconsistent performance predictions. Due to such high inherent variability, this factor is typically assigned a lower design weight while identifying the optimal mix proportion for NGA/MRA blends (discussed later in Section ↱3.8). Apparent cohesion must also be used with caution for the design and analysis of geotechnical structures employing MRA, as it is generally mobilised only up to the peak state, after which interlocking and cementation bonds deteriorate [64].

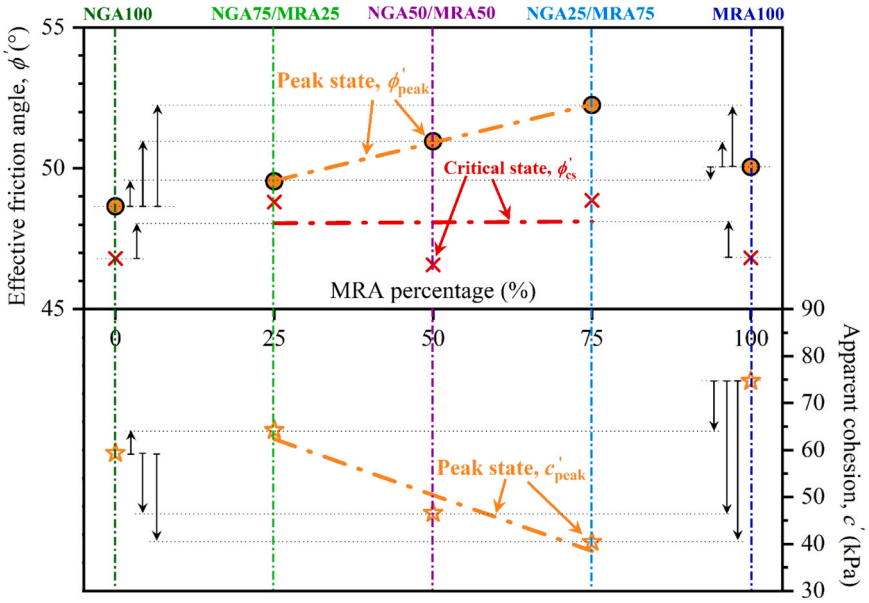

Fig. 11. Variation of peak and critical state friction angles and peak apparent cohesion with MRA percentage.

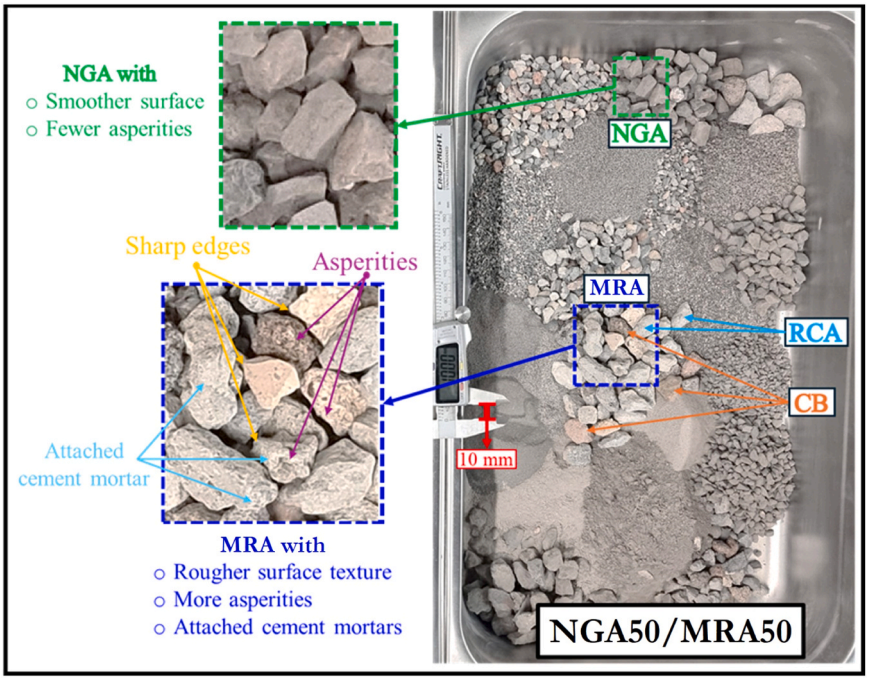

Fig. 12. A typical NGA50/MRA50 mixture before compaction (inset shows morphological characteristics of NGA and MRA particles).

Finally, at peak state, it is more appropriate to assess shear strength within a more generic perspective of the Mohr–Coulomb framework, the basis from which the conventional peak strength parameters are derived. The failure envelopes for the parent materials and mixtures are depicted in Fig. 13. Compared to NGA100 and mixtures, MRA100 consistently demonstrates the highest peak shear strength across all normal stress levels. For effective normal stresses below 150 kPa, the results exhibit a narrower range of values and smaller deviations without a distinct trend. This could be attributed to the fact that at these lower normal stress levels, employing a linear failure envelope tends to overestimate the real apparent cohesion, as discussed above. For effective normal stresses exceeding 150 kPa, the mixtures exhibit a clear advantage over NGA100, approaching the peak shear strength of MRA100. This trend is particularly pronounced at normal effective stresses beyond 300 kPa, where the mixtures with different MRA content display superior shear strength compared to NGA100, which exhibits the lowest strength, while NGA25/MRA75 shows the highest shear strength.

3.7. Maximum dilation and excess friction angles, and Bolton's stress-dilatancy relationship

To provide a more fundamental, mechanism-based interpretation of the observed shear strength, Bolton's stress-dilatancy framework [87] is invoked. In this framework, the excess friction angle is defined as the difference between the peak and critical state friction angles ($\phi'_{ex} = \phi'_{peak} - \phi'_{cs}$), which is directly proportional to the rate of dilation

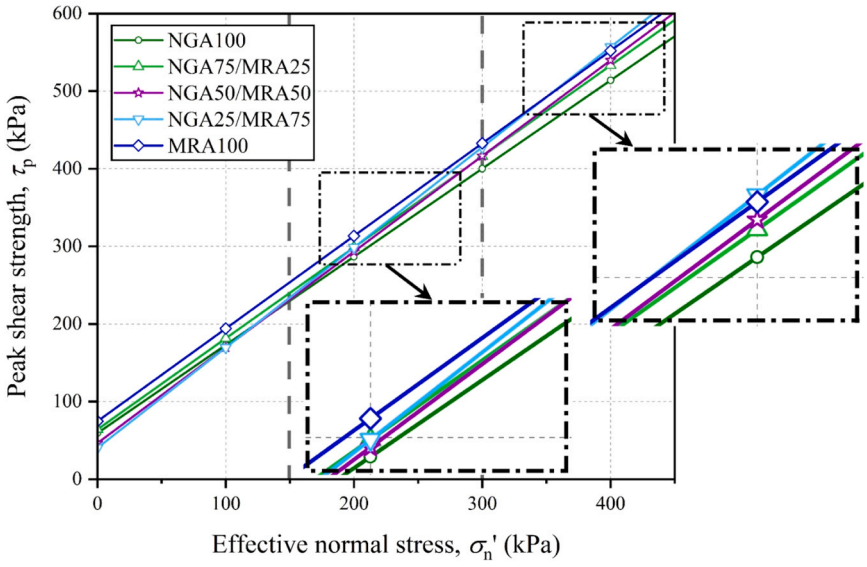

Fig. 13. Mohr–Coulomb failure envelopes for mixtures and their parent materials.

at failure, as follows:

$$\phi'_{peak} - \phi'_{cs} = b\psi_{max} \tag{8}$$

where b is Bolton's dilatancy index; ψ_{max} is the maximum dilation angle. This relationship underscores the importance of two key factors. One is the shear strength, which is linked to the critical state, and the other is the additional strength that arises from dilatancy. Both factors are essential for the development of the peak shear strength in granular materials [88]. The maximum dilation angle is defined as the highest value of the dilation angle (ψ), which is calculated as follows, according to Vermeer [89]:

$$\psi = \sin^{-1}\left(\frac{-\frac{d\varepsilon_v}{d\varepsilon_a}}{2-\left(\frac{d\varepsilon_v}{d\varepsilon_a}\right)}\right) \tag{9}$$

Fig. 14 illustrates the change in ψ_{max} and ϕ'_{ex} with σ'_3 and MRA percentage. The fitted response surfaces for ψ_{max} and ϕ'_{ex} exhibit similar trends for all the mixtures, indicating that the effects of varying MRA content and σ'_3 on ϕ'_{ex} are highly comparable to their effects on ψ_{max}. In other words, across changes in confining pressure and MRA content, the trend of change in maximum dilatancy mirrors the trend in excess friction angle. The presence of such a clear correspondence between ψ_{max} and ϕ'_{ex} validates the fundamental perspective that dilatancy and frictional behaviour in granular materials are intrinsically linked [90]. The corresponding values for ψ_{max} and ϕ'_{ex} are also provided in Table 3.

It can be observed from Fig. 14 that both ϕ'_{ex} and ψ_{max} increase with an increase in MRA content from 25% to 50%, followed by a reduction as MRA content rises from 50% to 75%. Thus, the NGA50/MRA50 mixture exhibits the highest level of ψ_{max} and ϕ'_{ex} among all mixtures. The parent materials define the bounds of the response for ψ_{max}, with NGA100 showing the lowest and MRA100 the highest values, respectively [Fig. 14(a)]. However, for ϕ'_{ex}, although MRA100 consistently exhibits the highest values across the range of σ'_3, NGA100 does not yield the lowest values; rather, the minima generally occur for the NGA75/MRA25 mixture [Fig. 14(b)]. This observation further validates the credibility of the analytical strategy presented in Section ↱3.1, which advocated for the exclusion of parent material data from the MRA content trend analysis for the mixtures, since including such data would have distorted the overall trajectory and obscured interpretive clarity.

Fig. 15 presents the relationship between ϕ'_{ex} and ψ_{max}, along with the values of the b index for each material, obtained via a linear fit. The value of b corresponding to NGA100 and NGA25/MRA75 is significantly different from other mixtures (NGA50/MRA50 and NGA75/MRA25) and MRA100. Fig. 16 illustrates the variation of the parameter b with MRA content. This parameter quantifies the extent to which the maximum dilatancy of the materials contributes to their ϕ'_{ex}. Given that ϕ'_{cs} for the NGA/MRA mixtures remains effectively constant (Fig. 11), the observed dependency on maximum dilatancy can, by inference, be expressed in ϕ'_{peak}. In fact, variations in dilatancy primarily modulate ϕ'_{peak} rather than ϕ'_{cs}. As can be seen in Fig. 16, compared to the mixtures, the parent material NGA100 exhibits the highest b value. As MRA content increases in the mixtures, b decreases (corresponding fitting equation is presented in Fig. 16), reaching a minimum value for the NGA25/MRA75 mixture, and then increases again for the parent material MRA100. Thus, NGA25/MRA75 shows the lowest b value across all mixtures, suggesting a transitional composition for this parameter.

As MRA content increases, ϕ'_{peak} rises (Fig. 11) while the contribution of dilatancy to peak strength (b) diminishes (Fig. 16). For the mixtures with greater MRA content, this reduced contribution of maximum dilatancy to peak friction may be associated with increased particle breakage of the weaker MRA fraction by NGA particles. Previous studies indicated that the crushability of materials influences dilatancy and its relationship with shear frictional characteristics [88]. Asadi et al. [91] indicated that while assemblies with higher angularity exhibit increased peak strength (and higher dilation at lower axial strains), the influence of particle breakage becomes more pronounced as axial strains rise, resulting in reduced dilation. Similarly, Chen et al. [92] observed that at high stress levels, the breakage of particles results in lower dilatancy rates.

3.8. Optimal mixture proportion

The method used in this study to find the optimal mixture is based on the Analytic Hierarchy Process (AHP), developed by Saaty [93], which is one of the most widely used Multi-Criteria Decision-Making (MCDM) tools in the construction industry, because it provides a comprehensive and rational framework for structuring a decision problem and quantifying its elements [94,95]. Five geotechnical properties were selected as the decision criteria for the process (see Table 5). The classification of each criterion is performed based on two distinct categories: "Benefit" criteria, characterised by higher values indicating favourable outcomes, and "Cost" criteria, where lower values are associated with better performance. ϕ'_{peak}, c'_{peak} and ϕ'_{cs} are considered as benefits since the

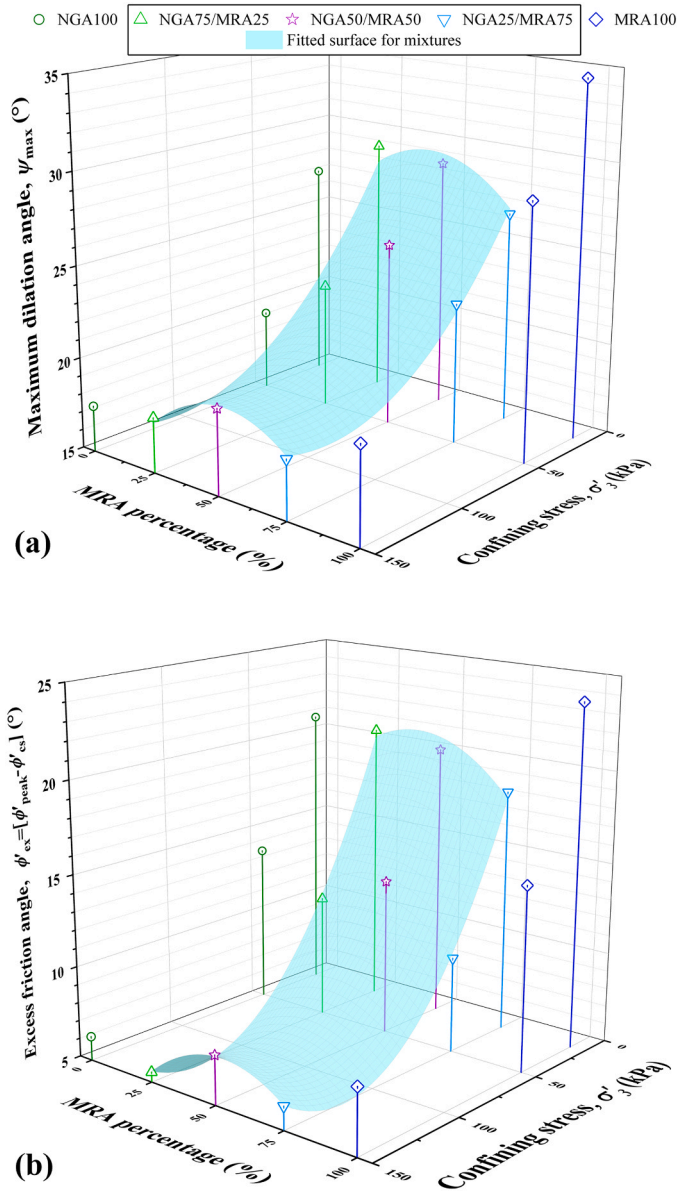

Fig. 14. Variation of (a) maximum dilation angle; and (b) excess friction angle with MRA percentage and confining stress.

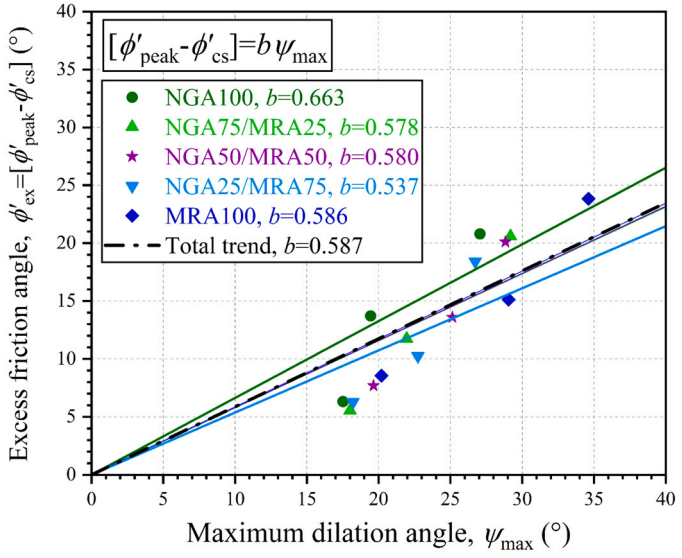

Fig. 15. Relationship between excess friction angle and maximum dilation angle.

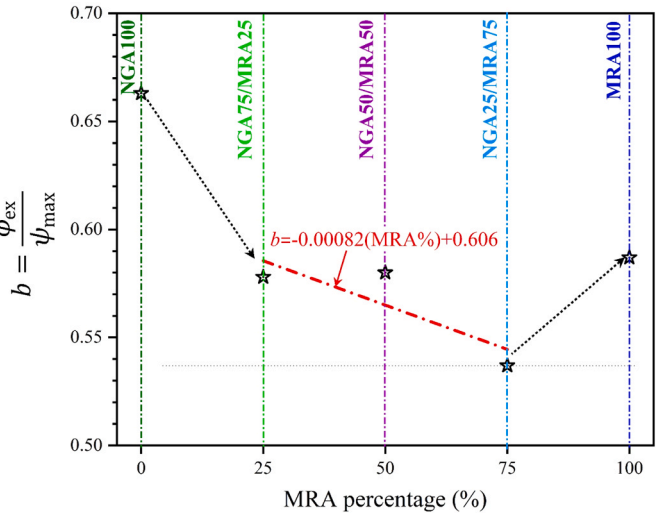

Fig. 16. Variation of parameter b with MRA content.

higher values of these parameters would be favourable in any geotechnical application. Conversely, SS and ψ_{max} are considered as costs since a ductile and less dilative material is more desirable for geotechnical applications, particularly in the transportation sector.

Within this evaluation framework, "Benefit" can reflect load-bearing capacity, whereas "Cost" penalises brittleness and volumetric instability that may compromise serviceability. Although dilation can elevate apparent peak strength, it is an unreliable strength measure given its sensitivity to several factors, such as mean effective stress, relative density, and crushing potential of aggregates [88,92,96]. In addition, shear strength is already captured by ϕ'_{peak}, c'_{peak} and ϕ'_{cs}. Accordingly, the maximum dilation angle ψ_{max} is treated as a "Cost" for its physical consequence, shear-induced volume change.

To enable a direct comparison of the values with different units (e.g., degrees versus kPa), normalisation is performed as a standard procedure in MCDM that converts every value to a common, dimensionless scale from 0 to 1. This allows for a fair comparison and weighting of each parameter. Thus, the values for each mixture are normalised, as represented in Table 5. The normalised value of each mixture for a given criterion, hereafter referred to as the performance score, is computed by scaling the observed value relative to the minimum and maximum values of that criterion across all mixtures, as described in the following equations:

Table 5
Performance score of parent materials and their mixtures for five different drained shear properties.

Materials	Performance score				
	ϕ'_{peak}	c'_{peak}	ϕ'_{cs}	SS	ψ_{max}
	Benefit	Benefit	Benefit	Cost	Cost
NGA100	0.000	0.553	0.100	1.000	1.000
NGA75/MRA25	0.246	0.695	0.972	0.306	0.741
NGA50/MRA50	0.641	0.180	0.000	0.580	0.517
NGA25/MRA75	1.000	0.000	1.000	0.918	0.816
MRA100	0.388	1.000	0.110	0.000	0.000

$$\text{For benefit criteria}: \text{ Performance score} = \frac{\text{Actual value} - \text{Minimum value}}{\text{Maximum value} - \text{Minimum value}} \quad (10)$$

$$\text{For cost criteria}: \text{ Performance score} = \frac{\text{Maximum value} - \text{Actual value}}{\text{Maximum value} - \text{Minimum value}} \quad (11)$$

Performance scores of 0 and 1 denote the least desirable and most favourable outcomes, respectively. Revisiting the results in preceding sections, NGA25/MRA75 demonstrated consistently favourable geotechnical behaviour, with higher ϕ'_{peak} and ϕ'_{cs}, alongside lower SS and ψ_{max}. In line with these observations, the corresponding performance scores of NGA25/MRA75 are relatively high for most criteria among all materials (see Table 5). The sole exception is c'_{peak}, for which NGA25/MRA75 exhibits a comparatively lower performance score, consistent with discussions in previous sections.

Building on previous analysis, the next stage entails a pairwise comparison of the criteria to establish their relative importance. Although all selected properties are essential for evaluation, their priority can vary with the target geotechnical application. In this study, three common applications of recycled MRA in road infrastructure are considered: pavement base materials [3–5,7], embankment fills [10–12], slope and retaining wall backfills [14,16,33].

The AHP procedure used to derive the pairwise comparison judgments is provided in Appendix A. In addition to the application-specific assessments, an application-neutral scenario is considered by assigning equal importance to all five criteria. This scenario provides the optimal mixture proportion solely based on results obtained in previous experiments without any biased direction. The resulting normalised weights for each criterion are listed in Table 6.

As discussed in Section ↱3.6, the inherent variability in MRA properties, combined with the nonlinearity of the peak shear strength failure envelope, requires a careful application of apparent cohesion in the design and analysis of geotechnical structures that utilise MRA. As a result of this limitation, a lower design weight is assigned to this factor when determining the optimal mix proportions for NGA/MRA blends, as illustrated in Table 6, which presents the criteria weights. Further details regarding the reduced importance of this factor in various applications in the pairwise comparison process can be found in Appendix A.

The overall score for each mixture is computed as a weighted sum of criterion-specific performance scores. Specifically, the normalised scores from Table 5 are multiplied by their corresponding criterion weights from Table 6, and then summed to calculate the overall scores for each mixture as:

$$\text{Overall score} = \sum_{i=1}^{5}(\text{Performance score}_i \times \text{Criterion weight}_i) \quad (12)$$

where i denotes the criteria.

Fig. 17(a) illustrates the final overall scores for the parent materials and their mixtures across various application scenarios. To assess the stability of the AHP rankings and account for potential uncertainties in criteria weight assignments, a Monte Carlo simulation was conducted. This simulation involved 10,000 iterations, during which the baseline weights for all criteria (presented in Table 6) were simultaneously subjected to random variations of up to ±20%. The outcomes of the Monte Carlo simulation, which present overall score ranges for each application, are displayed in Fig. 17(b), with the corresponding final overall rankings provided in Table 7. A higher overall score indicates superior performance, resulting in a higher rank for each respective application. The robustness and stability of the rankings for both NGA25/MRA75, ranked first, and MRA100, which typically ranks the lowest, are noteworthy.

Given the impact of uncertainties on the weighted criteria and the variations of the overall score for each application [see Fig. 17(b)], the NGA25/MRA75 mixture remained the top-performing alternative in 100% of iterations, with its score distribution consistently distinct from other alternatives, indicating high stability without overlap with other mixtures across all applications, and establishing it as the optimal mix proportion. In fact, NGA25/MRA75 retained the highest overall score across various application scenarios and uncertainties in weight criteria.

Initially, MRA100 may have appeared suitable due to its high peak shear strength (see Section ↱3.6). However, as demonstrated in Fig. 17, MRA100 generally exhibits the weakest overall performance, ranking lowest (see Table 7) across various applications. This trend is consistent, as MRA100 maintains its low rank with high stability despite uncertainties in weight criteria, leading to the conclusion that its standalone use is not recommended. The material exhibits pronounced strain softening, brittle behaviour, and substantial dilatancy potential. Therefore, blending MRA with NGA, preferably at a 75/25 ratio, is advisable to optimise shear-governed geotechnical performance while mitigating the limitations associated with pure MRA.

While the MRA utilised in this study was rigorously characterised (Table 1), it is important to note that real-world MRA streams exhibit significant compositional variability, which can influence mechanical performance. The effectiveness of MRA is primarily determined by the ratio of its two main components: RCA and CB. The batch analysed in this study contained approximately 16% CB, as indicated in Table 1. Prior research indicates that while RCA contributes to a robust and high-strength framework, attributed to the irregular shape and rough texture of crushed cement mortar, increasing the CB fraction beyond 25–30% can lead to reductions in shear strength and increased particle breakage under load due to the lower crushing resistance of clay bricks [25]. Additionally, the introduction of low-stiffness impurities, such as plastics or rubber, has been found to increase compressibility and lower the peak friction angle of the aggregate matrix [42]. Thus, the variability of these mixed materials, especially in their pure form, may result in high variability in the results. As demonstrated by the shear strength results discussed earlier, the inclusion of NGA effectively mitigates the shear strength and dilatancy properties within the waste stream (MRA). Thus, the blending strategy proposed in this study, which is mixing MRA with NGA, also offers a practical solution for the slight mitigation of the inherent variability in MRA quality. By providing a consistent, high-strength skeletal framework, the NGA component may reduce the sensitivity of the mixture to minor variations in MRA composition, such as slight increases in CB or levels of impurities. Consequently, the NGA25/MRA75 blend may demonstrate not only superior mechanical properties but also an enhanced safety profile in addressing the inherent heterogeneity of MRA compared to its standalone use. This is evidenced by the high performance of the blend, which remains robust even when accounting for variations of up to ±20% in the results, as assessed through Monte Carlo simulations to incorporate uncertainties.

Some studies investigated the cyclic behaviour of NGA/MRA mixtures, supporting the idea of incorporating substantial proportions of MRA into NGA [43,52,53]. Toka and Olgun [52] performed repeated loading tests on NGA/MRA mixtures for road base and subbase applications, concluding that MRA performs best when blended with NGA rather than when used in isolation. Their results identified

Table 6
Criteria weights for three geotechnical applications, alongside a neutral (unbiased) case.

Criteria	Criteria weights			
	Pavement base material	Embankment fill	Slope and retaining wall backfill	Neutral condition
ϕ'_{peak}	0.504	0.235	0.485	0.200
SS	0.260	0.528	0.204	0.200
ϕ'_{cs}	0.062	0.133	0.204	0.200
ψ_{max}	0.132	0.052	0.043	0.200
c'_{peak}	0.042	0.052	0.064	0.200

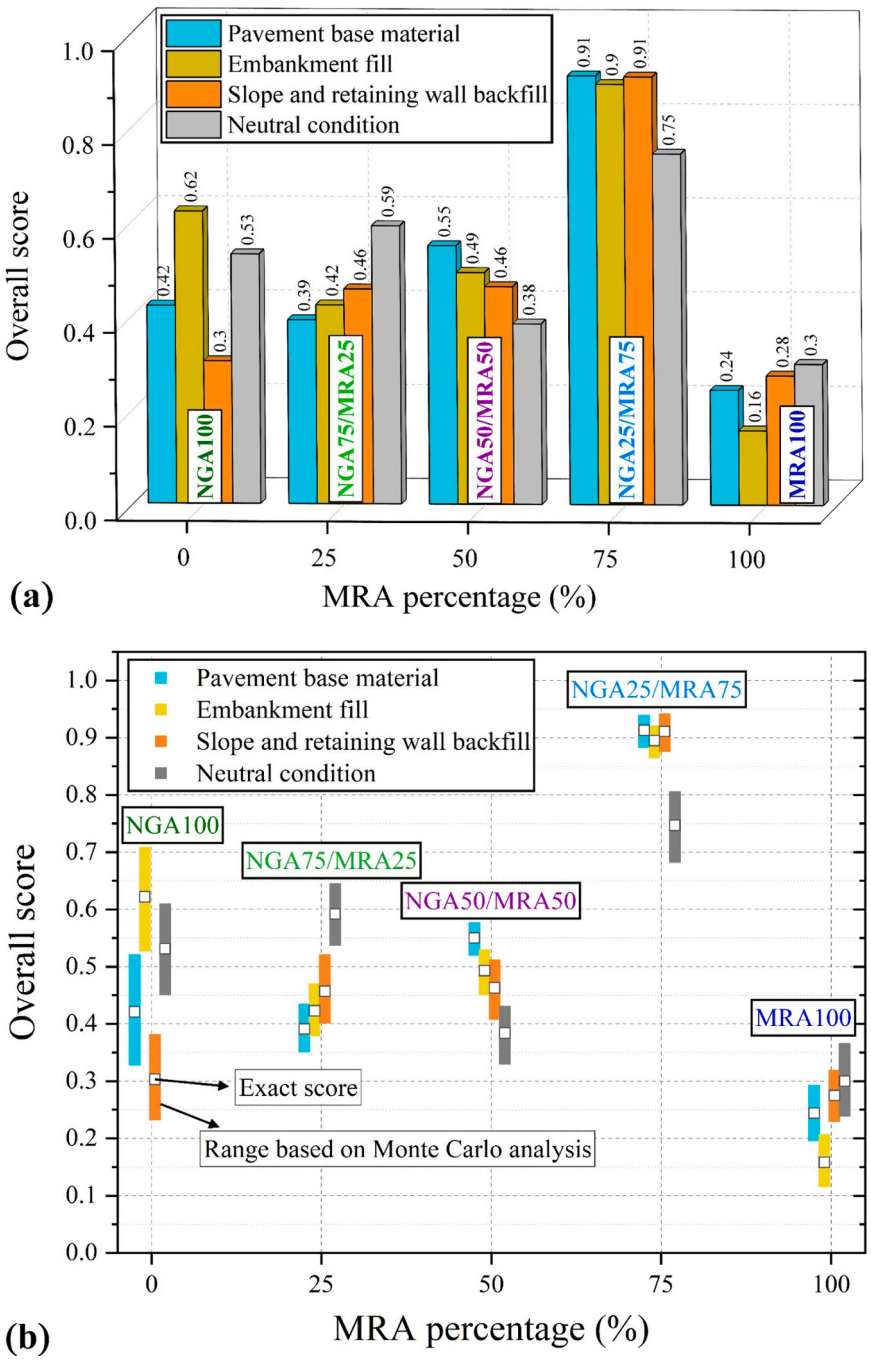

Fig. 17. (a) Overall scores (b) and their range based on Monte Carlo analysis, as a function of MRA content across three geotechnical applications and a neutral weighting condition.

NGA50/MRA50 as the most effective blend, followed by NGA25/MRA75, due to lower permanent deformation and higher resilient modulus (M_r). Likewise, Akbas and Iyisan [53] reported that NGA50/MRA50 and NGA25/MRA75 blends exhibited the highest stiffness and M_r under cyclic loading conditions and freeze-thaw cycles. Furthermore, Wang et al. [43] observed that the NGA15/MRA85 blend achieved a notably high M_r for embankment fill applications. Overall, the optimal MRA content identified in the present study falls within the range recommended in the literature, spanning from 50% to 85%, which was based on the response of such mixtures under cyclic loading.

4. Conclusions

The present study rigorously investigates the performance of mixed recycled aggregates (MRA) derived from construction and demolition waste (CDW), natural gravel aggregates (NGA) and their blends (NGA75/MRA25, NGA50/MRA50 and NGA25/MRA75), focusing specifically on their drained shear behaviour. The basic characterisation of NGA and MRA is first performed, followed by a series of consolidated drained monotonic triaxial tests to evaluate their key properties, such as peak shear strength, critical state friction angle, and the stress-dilatancy relationships. Furthermore, the effect of MRA content variation in NGA/MRA mixture on their drained shear strength and dilatancy characteristics is analysed under different confining pressures. It is important to

Table 7
Final overall ranks of NGA/MRA mixtures and parent materials across multiple geotechnical applications.

Material	Overall rank			
	Pavement base material	Embankment fill	Slope and retaining wall backfill	Neutral condition
NGA100	3, 4	2	4, 5	2, 3
NGA75/ MRA25	3, 4	3, 4	2, 3	2, 3
NGA50/ MRA50	2	3, 4	2, 3	4, 5
NGA25/ MRA75	1	1	1	1
MRA100	5	5	4, 5	4, 5

note that the observed behaviours of these materials are specific to the characteristics discussed in Section ↱2.1. Mixed recycled materials sourced from construction and demolition waste are highly variable, with properties that highly depend on their constituent materials, which can differ significantly based on the source. This inherent variability and uncertainty can also persist even within a single batch. The key findings of this study can be summarised as follows:

- MRA100 exhibited the highest soaked CBR value but experienced a significant drop in the unsoaked CBR value, indicating a high moisture sensitivity. The incorporation of NGA into MRA effectively mitigated this sensitivity, producing mixtures with comparable soaked and unsoaked CBR values. Among these, the NGA25/MRA75 mix stood out as the most stable composition, demonstrating high CBR values in both soaked and unsoaked conditions with minimal soaked-unsoaked CBR difference.
- Similar to NGA100, MRA100 and the mixtures demonstrated an increase in peak deviatoric stress (q_{peak}) and reduction in dilative volumetric strain with a rise in confining stresses (σ'_3). In addition, the axial strain corresponding to q_{peak} for the mixtures was consistently lower than that of NGA100 but higher than that of MRA100, with this trend being most evident in mixtures with lower MRA contents.
- The mixtures generally exhibited higher effective friction angles under peak (ϕ'_{peak}) and critical (ϕ'_{cs}) states compared to their parent materials. With increasing MRA percentage in the mixtures, ϕ'_{peak} increased while the peak apparent cohesion (c'_{peak}) decreased, and ϕ'_{cs} remained relatively constant.
- Despite possessing the highest c'_{peak} values, MRA100 exhibited the greatest strain softening (SS) and the highest maximum dilation angle (ψ_{max}) among all materials tested, suggesting potential limitations associated with its standalone use. However, these shortcomings can be addressed by mixing MRA with NGA, as the resulting mixtures exhibited more ductile behaviour (lower SS) and reduced dilatancy in comparison to MRA100, while achieving higher ϕ'_{peak} and ϕ'_{cs} than NGA100.
- Across variations in confining pressure and MRA content in the mixtures, the trend of change in maximum dilatancy mirrors the trend in excess friction angle.
- With rising MRA content in the mixtures, Bolton's dilatancy parameter decreased. This suggests that the mixtures with higher MRA percentages can mobilise greater ϕ'_{peak} despite having a lower contribution from dilatancy.
- Among all materials tested, NGA25/MRA75 is identified as the optimal mixture, consistently achieving the first rank based on key shear parameters including ϕ'_{peak}, ϕ'_{cs}, SS, and ψ_{max}. Except for lower c'_{peak}, this mixture demonstrated superior ductility compared to MRA100, characterised by reduced SS and a delayed attainment of the peak state, while maintaining shear strength fairly comparable to that of MRA100. This conclusion considers the variability of the materials and the impact of uncertainties within specified boundaries, as assessed through Monte Carlo analysis.

CRediT authorship contribution statement

Nariman Khorsandiardebili: Writing – original draft, Visualization, Methodology, Formal analysis, Data curation. **Sanjay Nimbalkar:** Writing – review & editing, Visualization, Supervision, Resources, Methodology, Funding acquisition, Conceptualization. **Piyush Punetha:** Writing – review & editing, Visualization, Supervision.

Declaration of Competing Interest

The authors declare that they have no known competing financial interests or personal relationships that could have appeared to influence the work reported in this paper

Acknowledgements

This research was financially supported by the SmartCrete CRC and industry partners: the Queensland Government Department of the Environment, Tourism, Science and Innovation, and the Scenic Rim Regional Council (Queensland, Australia), through the SmartCrete CRC Project 21.PP.0120 (2023). The first author gratefully acknowledges the financial support from the International Research Scholarship provided by the University of Technology Sydney.

Appendix A

To create a pairwise comparison matrix for each application, such as the pavement base, the significance of each criterion is compared against every other criterion, with a scale from 1 to 9, where 1 reflects no importance and 9 signifies extreme importance. It is essential to clarify that in the pairwise comparison matrix, the significance of each parameter is assessed for each row over those in the corresponding columns, as illustrated in Table 8. This methodology prioritises row parameters influencing the column parameters, rather than the reverse. For instance, as for the pavement base application in Table 8, the peak friction angle (ϕ'_{peak}) is rated as 5 "Strong Importance" over the maximum dilation angle (ψ_{max}). The sum of each column for each matrix is calculated and displayed in the last row of the pairwise comparison table (Table 8). Finally, each cell in the pairwise comparison matrix is divided by its respective column total to normalise the matrix, resulting in a new matrix where the sum of each column equals 1, as presented in Table 9. The subsequent sections elaborate on the three highest-priority geotechnical criteria for each application.

A.1. Pavement base

For the pavement bases, materials that exhibit higher ϕ'_{peak} were found to be more effective at resisting rutting [30,31], thereby contributing to the overall durability of pavements. The stability of pavement base materials arises from their ability to exhibit greater ductile behaviour, showing lower post-peak strength loss (characterised by SS) [64]. Additionally, the dilatancy of materials (ψ_{max}) plays a fairly significant role in predicting the plastic deformations during loading and unloading under repetitive loads [97].

A.2. Embankment fill

For embankments, the primary concern is global stability and the prevention of catastrophic progressive failure [98]. Therefore, minimising the potential for SS is the most critical criterion. ϕ'_{peak} for short-term stability and critical state strength (ϕ'_{cs}) for long-term stability are also key considerations [99].

A.3. Slope/retaining wall backfill

The design of a slope/retaining wall focuses on reducing active lateral earth pressure, which is inversely related to ϕ'_{peak} of the backfill, making this parameter critically important [100]. Additionally, for long-term safety, considerations must include ϕ'_{cs} and the prevention of post-peak strength loss (characterised by SS) [101].

A.4. Neutral condition

In the unbiased case, it is evident that no significance is assigned to any evaluating criteria relative to others, resulting in all criteria holding equal weight, devoid of any biased engineering judgments.

Table 8
Pairwise comparison matrix for evaluating criteria across various applications

Application	Criterion	ϕ'_{peak}	c'_{peak}	ϕ'_{cs}	SS	ψ_{max}
Pavement base	ϕ'_{peak}	1	8	7	3	5
	c'_{peak}	1/8	1	1/2	1/6	1/4
	ϕ'_{cs}	1/7	2	1	1/5	1/3
	SS	1/3	6	5	1	3
	ψ_{max}	1/5	4	3	1/3	1
	Sum	1.8	21	16.5	4.7	9.58
Embankment fill	ϕ'_{peak}	1	5	2	1/3	5
	c'_{peak}	1/5	1	1/3	1/8	1
	ϕ'_{cs}	1/2	3	1	1/5	3
	SS	3	8	5	1	8
	ψ_{max}	1/5	1	1/3	1/8	1
	Sum	4.9	18	8.67	1.78	18
Slope/retaining wall backfill	ϕ'_{peak}	1	7	3	3	8
	c'_{peak}	1/7	1	1/4	1/5	2
	ϕ'_{cs}	1/3	4	1	1	5
	SS	1/3	4	1	1	5
	ψ_{max}	1/8	1/2	1/5	1/5	1
	Sum	1.93	16.5	5.45	5.4	21

Note: "/" denotes a fraction.

Table 9
Normalisation and final weight calculation for evaluating criteria across various applications

Application	Criterion	ϕ'_{peak}	SS	ψ_{max}	ϕ'_{cs}	c'_{peak}	Sum	Final weight
Pavement base	ϕ'_{peak}	0.555	0.638	0.522	0.424	0.381	2.520	0.504
	SS	0.185	0.213	0.313	0.303	0.286	1.300	0.260
	ψ_{max}	0.111	0.071	0.104	0.182	0.190	0.659	0.132
	ϕ'_{cs}	0.079	0.043	0.035	0.061	0.095	0.312	0.062
	c'_{peak}	0.069	0.035	0.026	0.030	0.048	0.209	0.042
	Sum	1.000	1.000	1.000	1.000	1.000	5.000	1.000
Embankment fill	ϕ'_{peak}	0.561	0.612	0.577	0.444	0.444	2.639	0.528
	SS	0.187	0.204	0.231	0.278	0.278	1.177	0.235
	ψ_{max}	0.112	0.102	0.115	0.167	0.167	0.663	0.133
	ϕ'_{cs}	0.070	0.041	0.038	0.056	0.056	0.260	0.052
	c'_{peak}	0.070	0.041	0.038	0.056	0.056	0.260	0.052
	Sum	1.000	1.000	1.000	1.000	1.000	5.000	1.000
Slope/retaining wall backfill	ϕ'_{peak}	0.517	0.550	0.550	0.424	0.381	2.423	0.485
	SS	0.172	0.183	0.183	0.242	0.238	1.020	0.204
	ψ_{max}	0.172	0.183	0.183	0.242	0.238	1.020	0.204
	ϕ'_{cs}	0.074	0.046	0.046	0.061	0.095	0.321	0.064
	c'_{peak}	0.065	0.037	0.037	0.030	0.048	0.216	0.043
	Sum	1.000	1.000	1.000	1.000	1.000	5.000	1.000

Data availability

Data will be made available on request.

References

[1] P. Punetha, S. Nimbalkar, Utilisation of construction and demolition waste and recycled glass for sustainable flexible pavements: a critical review, Transp. Geotech. 50 (2025) 101612, https://doi.org/10.1016/j.trgeo.2025.101612.

[2] J. Pickin, C. Wardle, K. O'Farrell, P. Nyunt, S. Donovan, National waste report, Melbourne, Australia, (2020).
[3] K. Chiranjeevi, R. Yatish, D.H. Kumar, R.H. Mulangi, A.R. Shankar, Utilization of recycled concrete aggregates for pavement base courses–a detailed laboratory study, Constr. Build. Mater. 411 (2024) 134122, https://doi.org/10.1016/j.conbuildmat.2023.134122.
[4] L. Delongui, M. Matuella, W.P. Núñez, W. Fedrigo, L.C. da Silva Filho, J.A. P. Ceratti, Construction and demolition waste parameters for rational pavement design, Constr. Build. Mater. 168 (2018) 105–112, https://doi.org/10.1016/j.conbuildmat.2018.02.086.
[5] D. Xuan, A. Molenaar, L. Houben, Evaluation of cement treatment of reclaimed construction and demolition waste as road bases, J. Clean. Prod. 100 (2015) 77–83, https://doi.org/10.1016/j.jclepro.2015.03.033.
[6] G.T. Mehrjardi, A. Azizi, A. Haji-Azizi, G. Asdollafardi, Evaluating and improving the construction and demolition waste technical properties to use in road construction, Transp. Geotech. 23 (2020) 100349, https://doi.org/10.1016/j.trgeo.2020.100349.
[7] G. Liu, X. Luo, Y. Zhang, H. Li, Predicting fatigue damage growth in cement-treated base layer built with construction and demolition waste, Constr. Build. Mater. 406 (2023) 133371, https://doi.org/10.1016/j.conbuildmat.2023.133371.
[8] Z.A. Khan, U. Balunaini, S. Costa, N.H. Nguyen, A review on sustainable use of recycled construction and demolition waste aggregates in pavement base and subbase layers, Clean. Mater. 13 (2024) 100266, https://doi.org/10.1016/j.clema.2024.100266.
[9] X. Luo, G. Liu, Y. Zhang, T. Meng, L. Zhan, Estimation of resilient modulus of cement-treated construction and demolition waste with performance-related properties, Constr. Build. Mater. 283 (2021) 122107, https://doi.org/10.1016/j.conbuildmat.2020.122107.
[10] L. Liu, Z. Li, G. Cai, X. Geng, B. Dai, Performance and prediction of long-term settlement in road embankments constructed with recycled construction and demolition waste, Acta Geotech. 17 (2022) 4069–4093, https://doi.org/10.1007/s11440-022-01473-0.
[11] A. Soleimanbeigi, T.B. Edil, Compressibility of recycled materials for use as highway embankment fill, J. Geotech. Geoenviron. Eng. 141 (2015) 04015011, https://doi.org/10.1061/(asce)gt.1943-5606.0001285.
[12] J. Zhang, F. Gu, Y. Zhang, Use of building-related construction and demolition wastes in highway embankment: laboratory and field evaluations, J. Clean. Prod. 230 (2019) 1051–1060, https://doi.org/10.1016/j.jclepro.2019.05.182.
[13] Q.F. Gao, X.K. Shi, Z. Li, Z.N. Shi, L. Zeng, C.S. Wang, Seepage erosion and stability criterion for construction and demolition waste particles in embankment fill applications, J. Mater. Civ. Eng. 37 (2025) 04025422, https://doi.org/10.1061/jmcee7.mteng-20616.
[14] K. Fifer Bizjak, B. Likar, Validation of the recycled backfill material for the landslide stabilization at a railway line, Sci. Rep. 14 (2024) 7031, https://doi.org/10.1038/s41598-024-57555-4.
[15] E.C. Santos, E.M. Palmeira, R.J. Bathurst, Behaviour of a geogrid reinforced wall built with recycled construction and demolition waste backfill on a collapsible foundation, Geotext. Geomembr. 39 (2013) 9–19, https://doi.org/10.1016/j.geotexmem.2013.07.002.
[16] J. Muktinutalapati, A. GuhaRay, Earth pressures on retaining walls backfilled with sand admixed with building derived materials: laboratory scale study, Int. J. Geomech. 21 (2021) 04021072, https://doi.org/10.1061/(asce)gm.1943-5622.0002030.
[17] S.M. Tafreshi, A.A. Khanjani, A.R. Dawson, A. Faramarzi, Performance of recycled waste aggregate mixed with crushed glass over a weak subgrade, Constr. Build. Mater. 402 (2023) 133002, https://doi.org/10.1016/j.conbuildmat.2023.133002.
[18] J. Li, Y. Qin, J. Zhang, A. Zhang, X. Zhang, Compaction and shear characteristics of recycled construction & demolition aggregates in subgrade: exploring particle breakage and shape effects, J. Clean. Prod. 465 (2024) 142776, https://doi.org/10.1016/j.jclepro.2024.142776.
[19] Z. Duan, S. Zhang, W. Hou, C.S. Poon, Early-stage water-absorbing behavior and mechanism of recycled coarse aggregate, Constr. Build. Mater. 394 (2023) 132138.
[20] C. Shi, Y. Li, J. Zhang, W. Li, L. Chong, Z. Xie, Performance enhancement of recycled concrete aggregate–a review, J. Clean. Prod. 112 (2016) 466–472, https://doi.org/10.1016/j.jclepro.2015.08.057.
[21] C.S. Poon, X.C. Qiao, D. Chan, The cause and influence of self-cementing properties of fine recycled concrete aggregates on the properties of unbound sub-base, Waste Manag. 26 (2006) 1166–1172, https://doi.org/10.1016/j.wasman.2005.12.013.
[22] C. Wang, C. Chazallon, S. Braymand, P. Hornych, Influence of self-cementing properties on the mechanical behaviour of recycled concrete aggregates under monotonic loading, Constr. Build. Mater. 367 (2023) 130259, https://doi.org/10.1016/j.conbuildmat.2022.130259.
[23] A. Amin, A. Hasnat, A. Khan, M. Ashiquzzaman, Residual cementing property in recycled fines and coarse aggregates: occurrence and quantification, J. Mater. Civ. Eng. 28 (2016) 04015174, https://doi.org/10.1061/(asce)mt.1943-5533.0001472.
[24] C. Wang, C. Chazallon, P. Hornych, S. Mouhoubi, P. Jing, Effect of self-cementing properties on the resilient behaviour of recycled concrete aggregates used in base and subbase, Road. Mater. Pavement Des. 25 (2024) 2208–2224, https://doi.org/10.1080/14680629.2024.2302804.
[25] A. Arulrajah, J. Piratheepan, M. Bo, N. Sivakugan, Geotechnical characteristics of recycled crushed brick blends for pavement sub-base applications, Can. Geotech. J. 49 (2012) 796–811, https://doi.org/10.1139/t2012-041.
[26] Q. Ma, Z. Hu, Z. Hu, J. Li, Strength characteristics and micro-scale mechanism of high liquid limit clay treated by recycled construction and demolition wastes (CDW) aggregates, Constr. Build. Mater. 332 (2022) 127367, https://doi.org/10.1016/j.conbuildmat.2022.127367.
[27] J. Zhang, C. Li, L. Ding, J. Li, Performance evaluation of cement stabilized recycled mixture with recycled concrete aggregate and crushed brick, Constr. Build. Mater. 296 (2021) 123596, https://doi.org/10.1016/j.conbuildmat.2021.123596.
[28] A. Arulrajah, M.M. Disfani, S. Horpibulsuk, C. Suksiripattanapong, N. Prongmanee, Physical properties and shear strength responses of recycled construction and demolition materials in unbound pavement base/subbase applications, Constr. Build. Mater. 58 (2014) 245–257, https://doi.org/10.1016/j.conbuildmat.2014.02.025.
[29] A. Arulrajah, J. Piratheepan, M.M. Disfani, M.W. Bo, Geotechnical and geoenvironmental properties of recycled construction and demolition materials in pavement subbase applications, J. Mater. Civ. Eng. 25 (2013) 1077–1088, https://doi.org/10.1061/(asce)mt.1943-5533.0000652.
[30] M. Saberian, S.T.A.M. Perera, J. Li, J. Zhu, G. Wang, Effect of crushed glass on the shear behavior of recycled unbound granular aggregates incorporating crumb rubber, Int. J. Pavement Res. Technol. 15 (2022) 1079–1092, https://doi.org/10.1007/s42947-021-00073-7.
[31] W.J. Kim, H.J. Lee, H.T. Phan, Calibration and validation of a rutting model based on shear stress to strength ratio for asphalt pavements, Constr. Build. Mater. 149 (2017) 327–337, https://doi.org/10.1016/j.conbuildmat.2017.05.053.
[32] E. Santos, E. Palmeira, R. Bathurst, Performance of two geosynthetic reinforced walls with recycled construction waste backfill and constructed on collapsible ground, Geosynth. Int. 21 (2014) 256–269, https://doi.org/10.1680/gein.14.00013.
[33] C.S. Vieira, P.M. Pereira, M. de Lurdes Lopes, Recycled construction and demolition wastes as filling material for geosynthetic reinforced structures. Interface properties, J. Clean. Prod. 124 (2016) 299–311, https://doi.org/10.1016/j.jclepro.2016.02.115.
[34] M.P. Secco, G.J. Bruschi, C.S. Vieira, N. Cristelo, Geomechanical behaviour of recycled construction and demolition waste submitted to accelerated wear, Sustainability 14 (2022) 6719, https://doi.org/10.3390/su14116719.
[35] M.A. Farooq, S. Nimbalkar, Laboratory and numerical analyses on polyurethane–scrap rubber-reinforced base layer, Can. Geotech. J. 61 (2024) 2266–2285, https://doi.org/10.1139/cgj-2023-0583.
[36] Y. Xiao, H. Yang, Q. Fang, Y. Ling, H. Liu, Effect of shape discrepancies on strength of binary soils, Transp. Geotech. 50 (2025) 101609, https://doi.org/10.1016/j.trgeo.2025.101609.
[37] M.A. Farooq, S. Nimbalkar, Monotonic and cyclic triaxial testing of untreated and polyurethane-treated soil and soil–rubber mixtures, Acta Geotech. 19 (2024) 605–630, https://doi.org/10.1007/s11440-023-02100-2.
[38] J. Zhang, J. Yang, Experimental and numerical investigation of dilation behavior of asphalt mixture, Int. J. Geomech. 17 (2017) 04016062, https://doi.org/10.1061/(asce)gm.1943-5622.0000738.
[39] Y. Yilmaz, Y. Deng, C.S. Chang, A. Gokce, Strength–dilatancy and critical state behaviours of binary mixtures of graded sands influenced by particle size ratio and fines content, Geotechnique 73 (2023) 202–217, https://doi.org/10.1680/jgeot.20.p.320.
[40] S. Sarkar, A. Hegde, Stress–dilatancy and critical-state behavior of geogrid-reinforced recycled waste materials, J. Hazard. Toxic. Radioact. Waste 28 (2024) 04023042, https://doi.org/10.1061/jhtrbp.hzeng-1257.
[41] H. Yang, F. Zhao, J. Zhang, K. Liu, Numerical discrete element method investigation on mechanical properties of construction and demolition wastes within the critical state soil mechanics framework, Case Stud. Constr. Mater. 22 (2025) e04804, https://doi.org/10.1016/j.cscm.2025.e04804.
[42] M. Naeini, A. Mohammadinia, A. Arulrajah, S. Horpibulsuk, Stress-dilatancy responses of recovered plastics and demolition waste blends as a construction material, Constr. Build. Mater. 297 (2021) 123762, https://doi.org/10.1016/j.conbuildmat.2021.123762.
[43] Z. Wang, Y. Xiao, U.F. Aminu, Q. He, Y. Li, W. Li, Prediction of resilient modulus and critical dynamic stress of recycled aggregates: experimental study and machine learning methods, Transp. Geotech. 49 (2024) 101363, https://doi.org/10.1016/j.trgeo.2024.101363.
[44] X. Zhi, et al., Modeling the dynamic behavior of recycled concrete aggregate-virgin aggregates blend using artificial neural network, Sustainability 15 (2023) 14228, https://doi.org/10.3390/su151914228.
[45] DTMR, Materials Testing Manual. Queensland Government Department of Transport and Main Roads, Brisbane, Australia, 2023.
[46] B. Aytekin, A. Mardani, Y.S. Ünsever, Performance assessment of recycled waste materials for use in unbound pavement layers: a case study from Turkey, Constr. Build. Mater. 402 (2023) 133004, https://doi.org/10.1016/j.conbuildmat.2023.133004.
[47] DTMR, MRTS05 Unbound pavements. Queensland Government Department of Transport and Main Roads, Brisbane, Australia, 2022.
[48] SRRC, Gravel type 4.5 specification summary, Scenic Rims Regional Council, QLD, Australia 2023.
[49] AS 1141.5. Method for sampling and testing aggregates, method 5: particle density and water absorption of fine aggregate, Standards Australia, Sydney, Australia, 2018.

[50] AS 1141.6.1, Methods for sampling and testing aggregates, method 6.1: particle density and water absorption of coarse aggregate - weighing-in-water method, Standards Australia, Sydney, Australia, 2020.
[51] P. Kasinikota, D.D. Tripura, Evaluation of compressed stabilized earth block properties using crushed brick waste, Constr. Build. Mater. 280 (2021) 122520, https://doi.org/10.1016/j.conbuildmat.2021.122520.
[52] E.B. Toka, M. Olgun, Performance of granular road base and sub-base layers containing recycled concrete aggregate in different ratios, Int. J. Pavement Eng. 23 (2022) 3729–3742, https://doi.org/10.1080/10298436.2021.1916819.
[53] M. Akbas, R. Iyisan, Sustainable infrastructure: the effect of freeze-thaw cycles on road base materials comprising natural and recycled concrete aggregates, Int. J. Sustain. Eng. 16 (2023) 211–223, https://doi.org/10.1080/19397038.2023.2254564.
[54] ASTM D7181-20, Standard test method for consolidated drained triaxial compression test for soils, ASTM International, West Conshohocken, PA, 2020, https://doi.org/10.1520/d7181-20.
[55] L. Zhao, M. Deng, S. Zhang, D. Huang, N. Qiao, J. Gong, Effects of particle shape on triaxial compression behaviours of realistic ballast particles based on MAVL particle shape evaluation system, Granul. Matter 25 (2023) 4, https://doi.org/10.1007/s10035-022-01288-6.
[56] J. Duan, J. Wu, Y. Su, Y. Lin, Y. Li, L. Lu, Shear behaviors of expansive soils over a wide confining pressures range and their impacts on strength parameters, Transp. Geotech. 48 (2024) 101328, https://doi.org/10.1016/j.trgeo.2024.101328.
[57] J. Zhang, A. Zhang, J. Li, H. Fan, Enhanced understanding on permanent deformation behaviour of subgrade compacted clay under long-term cyclic loading, Soil Dyn. Earthq. Eng. 187 (2024) 108972, https://doi.org/10.1016/j.soildyn.2024.108972.
[58] T. Park, Application of construction and building debris as base and subbase materials in rigid pavement, J. Transp. Eng. 129 (2003) 558–563, https://doi.org/10.1061/(asce)0733-947x(2003)129:5(558).
[59] M.J. Martinez-Echevarria, et al., Crushing treatment on recycled aggregates to improve their mechanical behaviour for use in unbound road layers, Constr. Build. Mater. 263 (2020) 120517, https://doi.org/10.1016/j.conbuildmat.2020.120517.
[60] W.F. Jin, J.J. Xie, Y. Tao, Y.H. Ma, Opposite turning hook of crushable sand's stress–dilatancy curve and its prediction, Acta Geotech. 19 (2024) 3621–3636, https://doi.org/10.1007/s11440-023-02150-6.
[61] X.S. Li, Y.F. Dafalias, Dilatancy for cohesionless soils, Geotechnique 50 (2000) 449–460, https://doi.org/10.1680/geot.2000.50.4.449.
[62] X. Wang, J. Cui, W. Wang, Dilatancy behaviors of calcareous sand considering particle breakage, Bull. Eng. Geol. Environ. 83 (2024) 146, https://doi.org/10.1007/s10064-024-03618-9.
[63] S.A. Harehdasht, M. Karray, M.N. Hussien, M. Chekired, Influence of particle size and gradation on the stress-dilatancy behavior of granular materials during drained triaxial compression, Int. J. Geomech. 17 (2017) 04017077, https://doi.org/10.1061/(asce)gm.1943-5622.0000951.
[64] A. Buritatum, et al., Evaluation of shear strength improvement of recycled concrete aggregate as a high-quality pavement material utilizing CO2 carbonation treatment, Constr. Build. Mater. 489 (2025) 142193, https://doi.org/10.1016/j.conbuildmat.2025.142193.
[65] N.C. Consoli, R.C. Cruz, A.V. Da Fonseca, M.R. Coop, Influence of cement-voids ratio on stress-dilatancy behavior of artificially cemented sand, J. Geotech. Geoenviron. Eng. 138 (2012) 100–109, https://doi.org/10.1061/(asce)gt.1943-5606.0000565.
[66] A. Gluchowski, M. Iskander, Evolution of particle breakage during cyclic shear of sand, Granul. Matter 27 (2025) 1–21, https://doi.org/10.1007/s10035-025-01548-1.
[67] J.H. Shen, X. Wang, J. Cui, X.Z. Wang, C.Q. Zhu, Shear characteristics of calcareous gravelly sand considering particle breakage, Bull. Eng. Geol. Environ. 81 (2022) 130, https://doi.org/10.1007/s10064-022-02603-4.
[68] R. Nova, D.M. Wood, A constitutive model for soil under monotonic and cyclic loading, Soil Mech. Transient Cycl. Load. (1982) 343–373.
[69] H. He, et al., Characterization of recycled concrete aggregate (RCA) particles for geotechnical engineering applications: particle strength and interparticle contact behavior, Constr. Build. Mater. 407 (2023) 133532, https://doi.org/10.1016/j.conbuildmat.2023.133532.
[70] P. Mikhailenko, Z. Piao, M.R. Kakar, M. Bueno, L.D. Poulikakos, Durability and surface properties of low-noise pavements with recycled concrete aggregates, J. Clean. Prod. 319 (2021) 128788, https://doi.org/10.1016/j.jclepro.2021.128788.
[71] P. Vangla, M.L. Gali, Effect of particle size of sand and surface asperities of reinforcement on their interface shear behaviour, Geotext. Geomembr. 44 (2016) 254–268, https://doi.org/10.1016/j.geotexmem.2015.11.002.
[72] P. Punetha, P. Mohanty, M. Samanta, Microstructural investigation on mechanical behavior of soil-geosynthetic interface in direct shear test, Geotext. Geomembr. 45 (2017) 197–210, https://doi.org/10.1016/j.geotexmem.2017.02.001.
[73] J.H. Pan, J.M. Zhang, R. Wang, Influence of small particle surface asperities on macro and micro mechanical behavior of granular material, Int. J. Numer. Anal. Methods Geomech. 46 (2022) 961–978, https://doi.org/10.1002/nag.3328.
[74] Z. Yang, J. Yang, L. Wang, On the influence of inter-particle friction and dilatancy in granular materials: a numerical analysis, Granul. Matter 14 (2012) 433–447, https://doi.org/10.1007/s10035-012-0348-x.
[75] A. Sadrekarimi, S. Olson, Critical state friction angle of sands, Geotechnique 61 (2011) 771–783, https://doi.org/10.1680/geot.9.p.090.
[76] P. Giovine, P.M. Mariano, G. Mortara, Micro to MACRO mathematical modelling in soil mechanics, Springer, 2019, https://doi.org/10.1007/978-3-319-99474-1.
[77] K. Senetakis, M.R. Coop, M.C. Todisco, The inter-particle coefficient of friction at the contacts of Leighton Buzzard sand quartz minerals, Soils Found. 53 (2013) 746–755, https://doi.org/10.1016/j.sandf.2013.08.012.
[78] J. Lackenby, B. Indraratna, G. McDowell, D. Christie, Effect of confining pressure on ballast degradation and deformation under cyclic triaxial loading, Geotechnique 57 (2007) 527–536, https://doi.org/10.1680/geot.2007.57.6.527.
[79] X. Zhu, L. Ding, Y. Wu, X. Wang, X. Tan, Effect of brick aggregate content on performance of recycled construction-solid-waste aggregate, Materials 17 (2024) 2616, https://doi.org/10.3390/ma17112616.
[80] S. Nimbalkar, B. Indraratna, S.K. Dash, D. Christie, Improved performance of railway ballast under impact loads using shock mats, J. Geotech. Geoenviron. Eng. 138 (2012) 281–294, https://doi.org/10.1061/(asce)gt.1943-5606.0000598.
[81] R. Baker, Nonlinear Mohr envelopes based on triaxial data, J. Geotech. Geoenviron. Eng. 130 (2004) 498–506, https://doi.org/10.1061/(asce)1090-0241(2004)130:5(498).
[82] D. Ling, T. Hu, J. Wang, X. Wang, C. Shi, Y. Tang, Numerical study on the shear strength of granular materials under the low confining pressure, Soils Found. 64 (2024) 101447, https://doi.org/10.1016/j.sandf.2024.101447.
[83] H. Yu, K. Ng, D. Grana, V. Alvarado, J. Kaszuba, E. Campbell, A generalized power-law criterion for rocks based on Mohr failure theory, Int. J. Rock. Mech. Min. Sci. 128 (2020) 104274, https://doi.org/10.1016/j.ijrmms.2020.104274.
[84] A. Azam, D. Cameron, Geotechnical properties of blends of recycled clay masonry and recycled concrete aggregates in unbound pavement construction, J. Mater. Civ. Eng. 25 (2013) 788–798, https://doi.org/10.1061/(asce)mt.1943-5533.0000634.
[85] M.G. Arab, M. Alzara, W. Zeiada, M. Omar, A. Azam, Combined effect of compaction level and matric suction conditions on flexible pavement performance using construction and demolition waste, Constr. Build. Mater. 261 (2020) 119792, https://doi.org/10.1016/j.conbuildmat.2020.119792.
[86] A. Arisha, A. Gabr, S. El-Badawy, S. Shwally, Performance evaluation of construction and demolition waste materials for pavement construction in Egypt, J. Mater. Civ. Eng. 30 (2018) 04017270, https://doi.org/10.1061/(asce)mt.1943-5533.0002127.
[87] M.D. Bolton, The strength and dilatancy of sands, Geotechnique 36 (1986) 65–78.
[88] Z.L. Dong, C.X. Tong, S. Zhang, Y.P. Cheng, D. Sheng, Strength and dilatancy of crushable soils with different gradings, Can. Geotech. J. 62 (2024) 1–21, https://doi.org/10.1139/cgj-2023-0554.
[89] P.A. Vermeer, Non-associated plasticity for soils, concrete and rock, in: H. J. Herrmann, J.P. Hovi, S. Luding (Eds.), Physics of Dry Granular Media, Springer, Dordrecht, 1998, pp. 163–196, https://doi.org/10.1007/978-94-017-2653-5_10.
[90] A.A. Ouici, A.C. Taiba, Y. Mahmoudi, M. Belkhatir, Influence of fines and gravel particles on strength-dilatancy of river sand: effect of depositional conditions, Mar. Georesour. Geotechnol. 43 (2025) 1388–1402, https://doi.org/10.1080/1064119x.2024.2409411.
[91] R. Asadi, M.M. Disfani, B. Ghahreman-Nejad, M.O. Ciantia, Effect of flexible membrane in triaxial test on the mechanical behaviour of rockfill material using discrete element method, Granul. Matter 26 (2024) 70, https://doi.org/10.1007/s10035-024-01441-3.
[92] C. Chen, Dk Wu, Y. Sun, X. Zhang, Macro-and-micromechanical responses of ballast under triaxial shearing using coupled DEM–FDM with flexible and rigid membranes: a comparative study, Granul. Matter 26 (2024) 42, https://doi.org/10.1007/s10035-024-01412-8.
[93] R.W. Saaty, The analytic hierarchy process–what it is and how it is used, Math. Model 9 (1987) 161–176, https://doi.org/10.1016/0270-0255(87)90473-8.
[94] D. Jato-Espino, E. Castillo-Lopez, J. Rodriguez-Hernandez, J.C. Canteras-Jordana, A review of application of multi-criteria decision making methods in construction, Autom. Constr. 45 (2014) 151–162, https://doi.org/10.1016/j.autcon.2014.05.013.
[95] M.M.A. Bhuiyan, A. Hammad, A hybrid multi-criteria decision support system for selecting the most sustainable structural material for a multistory building construction, Sustainability 15 (2023) 3128, https://doi.org/10.3390/su15043128.
[96] O. Cinicioglu, A. Abadkon, Dilatancy and friction angles based on in situ soil conditions, J. Geotech. Geoenviron. Eng. 141 (2015) 06014019, https://doi.org/10.1061/(asce)gt.1943-5606.0001272.
[97] M. Bahador, T. Evans, M. Gabr, Modeling effect of geocomposite drainage layers on moisture distribution and plastic deformation of road sections, J. Geotech. Geoenviron. Eng. 139 (2013) 1407–1418, https://doi.org/10.1061/(asce)gt.1943-5606.0000877.
[98] K. Briggs, F. Loveridge, S. Glendinning, Failures in transport infrastructure embankments, Eng. Geol. 219 (2017) 107–117, https://doi.org/10.1016/j.enggeo.2016.07.016.
[99] B. Xia, G. Zheng, H. Zhou, Y. Diao, Failure mechanisms and characteristics of high-filled embankments with different types of basal reinforcement, Transp. Geotech. 51 (2025) 101528, https://doi.org/10.1016/j.trgeo.2025.101528.
[100] M. Jiang, M. Niu, W. Zhang, DEM analysis of passive failure in structured sand ground behind a retaining wall, Granul. Matter 24 (2022) 61, https://doi.org/10.1007/s10035-022-01220-y.
[101] Y. Tang, W. Wu, K. Yin, S. Wang, G. Lei, A hydro-mechanical coupled analysis of rainfall induced landslide using a hypoplastic constitutive model, Comput. Geotech. 112 (2019) 284–292, https://doi.org/10.1016/j.compgeo.2019.04.024.